Supporting Information

In-situ Built Interphase with High Interface Energy and Fast Kinetics for High Performance Zn Metal Anodes

Yuzhu Chu, [a, b] Shu Zhang, [c] Shuang Wu, [b] Zhenglin Hu,*[b] Guanglei Cui [c] and Jiayan Luo*[a, b]

[a]*Shanghai Key Lab of Advanced High-Temperature Materials and Precision Forming, School of Materials Science and Engineering, Shanghai Jiao Tong University, Shanghai 200240, P. R. China.*

[b]*Key Laboratory for Green Chemical Technology of Ministry of Education, State Key Laboratory of Chemical Engineering, School of Chemical Engineering and Technology, Tianjin University Tianjin 300072, P. R. China.*

[c]*Qingdao Institute of Bioenergy and Bioprocess Technology, Chinese Academy of Sciences, Qingdao 266101, P. R. China.*

**Corresponding author. E-mail: huzl@tju.edu.cn (Z. H.), jyluo@sjtu.edu.cn (J. L.)*

Experimental Section

Preparation of MnO_2/CNT:

MnO_2/CNT was prepared according to the previous report.[1] The preparation process of MnO_2/CNT material is mainly divided into two steps: one is the acidizing treatment of multi-walled carbon nanotubes (CNT) (Nanjing XFNano Material Tech Co., Ltd)) and the other is the composite of CNT and α-MnO_2. Commercially used CNT was heated and refluxed in nitric acid (AR, Aladdin) at 80°C for 6 hours, and then washed using deionized water several times. 0.15 g acidified CNT and 2.94 g $Mn(CH_3COO)_2 \cdot 4H_2O$ (AR, Aladdin) were dispersed in 150 mL deionized water, and stirred continuously for 30 minutes to obtain mixed solution A. Subsequently, 80 mL aqueous solution containing 1.27 g of $KMnO_4$ was added dropwise to the mixed solution A, stirred for 30 minutes and then ultrasonically dispersed for 10 minutes to obtain the mixed solution B. After that, the mixed solution B was transferred to a polytetrafluoroethylene high-pressure steam reactor, and reacted at 120°C for 12 h. After natural cooling, the reactant was filtered, and the obtained dark brown precipitate was washed with deionized water several times, and dried in a vacuum oven at 80°C for 12 h to obtain α-MnO_2/CNT material.

Preparation of $Zn_3(PO_4)_2$-Zn and ZnF_2-Zn:

The pristine zinc foil was polished with sand paper before use.

$Zn_3(PO_4)_2$-Zn was obtained via the simple chemical reaction between Zn and $(NH_4)_2HPO_4$ aqueous solution. 10 pieces of Zn plates (φ = 12 mm) were immersed into 10 mL of 0.05 M $(NH_4)_2HPO_4$ (AR, Kermel) aqueous solution at mildly stirring for 5 h. Then the treated Zn plate was washed with deionized water and absolute ethyl alcohol for several times, and dried at 80°C finally.

According to the previous report,[2] NH_4F dispersed in dimethyl sulfoxide (DMSO) was used to treat Zn foil and obtain ZnF_2-Zn. 5.0 mg NH_4F (99.99%, Aladdin) was dissolved in 6 mL DMSO under vigorous stirring for 3 days. Then, 20 μL NH_4F solution was dropped on the surface of Zn plate (φ = 12 mm) and fast dried at 180 °C in glove box for 10 min. During this process, DMSO evaporated rapidly and NH_4F decomposed into HF and NH_3. The generated HF will react with Zn and produce ZnF_2 on the surface of Zn. This process was repeated for 10 times to obtain ZnF_2-Zn.

Preparation of MnO_2/CNT cathode and active carbon cathode:

MnO_2/CNT (70 wt%), Super P (20 wt%), and polyvinylidene fluoride (PVDF) (10 wt%) were mixed and dispersed in N-methyl pyrrolidone to form a slurry. Then the slurry was coated on carbon paper and dried in a vacuum oven at 80 ℃ for 12 h. The coated carbon paper was punched into disks (φ = 12 mm), which could be used as the cathodes for Zn|MnO_2 full cells. The cathodes for Zn-ions hybrid supercapacitors consisting of

active carbon (AC), Super P, and PVDF with a mass ratio of 7: 2: 1, were prepared by the similar procedure, except for the current collector for AC cathode was stainless steel foil (10 μm in thickness). The areal loading mass of MnO_2 was around 1.0 mg cm^{-2} and the loading of AC was around 2.0 mg cm^{-2}. It should be pointed out that the discharge capacity of Zn|MnO_2 full cells and Zn|AC hybrid supercapacitors is calculated based on the mass of active materials in cathode.

Characterization

Field emission scanning electron microscope (SEM, Hitachi S-4800) combined with energy dispersive X-ray spectroscopy (EDX) was used to detect the micro-morphology and elements distribution of samples. X-ray diffraction (XRD) characterization was conducted on Rigaku D/max-2500B2+/PCX device with Cu Kα irradiation. X-ray photoelectron spectroscopy (XPS, K-Alpha+) with an Al Kα source was used to analyze the chemical composition of the surface of Zn electrode. The microstructure of MnO_2/CNT and the lattice fringes of composite SEI mainly composed of $Zn_3(PO_4)_2$ and ZnF_2 (ZCS) were captured by JEM-2001F field-emission transmission electron microscope (TEM). Fourier transform infrared spectra (FTIR) was tested on a Nicolet iS10 (Thermo Electron Corp. USA) to further investigate the interphase composition induced by PF_6^-. It needs to be emphasized that PO_4^{3-} group has similar absorption peak location with SO_4^{2-} in $Zn_4SO_4(OH)_6{\cdot}xH_2O$, the typical

by-product of $ZnSO_4$ aqueous electrolyte and Zn metal.[3] Thus, H_2O and 0.05 M KPF_6 aqueous solution without $ZnSO_4$ salt were used to treat Zn foil for FTIR test. The absorption peaks of ZnF_2 can be obtained from the website database of www.organchem.csdb.cn. The contact angle between electrolyte and Zn foil with or without ZCS was measured by a contact angle goniometer (Ram´e Hart 260). Differential electrochemical mass spectrometry (DEMS) was used to quantitatively detect the gas (mainly H_2) generating during the resting process of Zn|Zn symmetric cells. Optical microscopy (RX50M China) was used to observe the plating process of Zn^{2+} in a home-made cell with a transparent window. To determine the CNT content in MnO_2/CNT, TGA curve was tested by TA Q50 with a heating rate of 10 °C min^{-1} from 50 to 800 °C in the air atmosphere. The bulk modulus (*E*) of different inorganic Zn-based compounds can be obtained from https://materialsproject.org.

Electrochemical measurements

The influence of ZCS on electrochemical performance of Zn anode was systemically evaluated using Zn|Zn symmetric cells, Zn|Ti asymmetric cells, Zn|MnO_2 full cells, and Zn|AC hybrid supercapacitors. All these cells were assembled to CR2032-type coin cells with a piece of glass fiber paper as the separator. The thickness of the Zn anodes used in this article is 100 μm unless otherwise specified. The electrolyte amounts of the Zn-based coin cells are controlled at 80 μL. Galvanostatic charge-

discharge (GCD) and Coulombic efficiency (CE) were measured on a LAND-CT2001A battery tester. For the GCD measurement of Zn|Zn symmetric cells, the cells were per-activated at 0.1 mA for 10 cycles (20 minutes per cycle), when the areal capacity is larger than 1 mA h cm^{-2}. CE was tested using Zn|Ti half-cells to measure the reversibility of Zn plating/stripping process. The batteries were first cycled for 5 cycles to promote the formation of ZCS on Ti foil, where Zn was plated for 10 min at each cycle under the current of 0.1 mA with cut-off voltage of 0.5 V. After the activation process, metal Zn with a fixed capacity was plated on Ti foil at a higher current density and then stripped away until the voltage up to 0.5 V. The CE is determined by the ratio of stripping to plating capacity during each cycle. Cyclic voltammetry (CV), Tafel corrosion curves, and electrochemical impedance spectroscopy (EIS) were conducted on Solartron Metrology. More specifically, CV of Zn plating/stripping were tested at a scan rate of 5 mV s^{-1} in a three-electrode configuration where Ti plate, Zn plate, Ag/AgCl (saturated KCl) were employed as working, counter and reference electrodes, respectively. Tafel corrosion curves were tested at a scan rate of 1 mV s^{-1} in a three-electrode configuration where Zn plate, Ti plate, Ag/AgCl (saturated KCl) were employed as working, counter and reference electrodes, respectively. The corrosion potential and corrosion current were calculated from Tafel fit system in electrochemical workstation. EIS was

carried out at an amplitude of 10 mV with a frequency ranging from 10^6 Hz to 0.01 Hz. To clarify the impact of ZCS layer on hydrogen evolution, linear sweep voltammetry (LSV) was used to investigate the HER on Zn anodes with and without ZCS layer in 1 M Na_2SO_4 aqueous electrolyte. The LSV measurement was carried out at a scan rate of 5 mV s^{-1} in a three-electrode configuration, where Zn plate with or without ZCS, Ti plate, and Ag/AgCl (saturated KCl) were used as working, counter, and reference electrodes, respectively.

The energy density E (W h kg^{-1}) and power density P (W kg^{-1}) of ZHCs can be calculated according to equations:

$$E = \int_{t_1}^{t_2} IVdt \qquad \text{Equation(S1)}$$

Where I (A kg^{-1}) is the constant current density; V (V) is the voltage; t_1 and t_2 (h) is the start and end time of the discharge process, respectively.

$$P = \frac{E}{\Delta t} \qquad \text{Equation(S2)}$$

Where Δt (h) is discharge time. It should be noted that the energy density and power density are calculated based on the mass of active materials in cathodes.

The ionic conductivity of the ZCS layer (Fig. 2g) was calculated according to the following equation:[4]

$$\sigma = 2\pi f_{\max} \varepsilon_0 \varepsilon_r \qquad \text{Equation(S3)}$$

where σ represents the ionic conductivity of the in-situ ZCS layer, ε_0 is the permittivity of free space (8.9×10^{-12} F/m), and ε_r is the permittivity

of ZCS layer (≈10.0 F/m).

The transference number of Zn^{2+} ($T_{Zn^{2+}}$) was tested in Zn|Zn symmetrical cells by EIS before and after the chronoamperometry (CA) tests and calculated by the following equation:

$$T_{Zn^{2+}} = \frac{I_s(\Delta V - I_0 R_0)}{I_0(\Delta V - I_s R_s)} \quad \text{Equation(S4)}$$

where ΔV is the applied voltage polarization, I_s and R_s are the steady state current and resistance, respectively, and I_0 and R_0 are the initial current and resistance, respectively. Here, the applied voltage polarization is 5 mV (Fig. S15).

Zn^{2+} deposition barrier could be quantitatively evaluated based on the temperature-dependent EIS (Fig. S17 and Fig. 3c), according to the following equation:[5-8]

$$\ln(Rct^{-1}) = \ln A - E_a / RT \quad \text{Equation(S5)}$$

Where R_{ct} is the interfacial Zn^{2+} transfer resistance, E_a is the activation energy, T is the absolute temperature, R is the gas constant, and A is the pre-exponential factor.

The exchange current density for hydrogen evolution reaction (HER) was calculated based on the linear sweep voltammetry (LSV) of Zn in 1 M Na_2SO_4 (Fig. S20b). The relationship between the overpotential (η) and current in logarithmic format (log (*i*)) obeys the Tafel equation:

$$\eta = a + b\log(i) \quad \text{Equation(S6)}$$

Where a and b are Tafel parameters, representing the intercept and slope,

respectively. When overpotential (η) is reached 0 V, the corresponding current density is the exchange current density of hydrogen evaluation (I_{H_2}), which could be obtained by fitting the linear portion of Tafel plot (Fig. S20c). The fitting results of a and b are listed in Table S6.

The energy storage mechanism of Zn|MnO_2-CNT full cells was investigated based on the CV curves at various scan rates (Fig. 5a and Fig. S32a). The relationship between peak current density (i) and scan rate(v) could be expressed by the following equation:

$$i = av^b \qquad \text{Equation(S7)}$$

where both a and b are adjustable parameters. The value of b can be obtained by fitting the slope of the log (i) vs. log (v) plot (Fig. 5b and Fig. S32b). Generally, when b = 0.5, the energy storage mechanism corresponds to a diffusion-controlled process (a battery-like mechanism); When b = 1, the energy storage is controlled by surface capacitance (a capacitor-like mechanism).[9, 10]

DFT Calculations

The first-principles calculations based on density functional theory (DFT) were conducted using VASP package. The interfacial energy ($\gamma_{Zn\text{-}b}$) between Zn metal and component b was calculated as follows:[11, 12]

$$\gamma_{Zn\text{-}b}(\Omega, n_b) = \frac{E_{Zn\text{-}b}(\Omega, A, n_{Zn}, n_b) - n_{Zn}E_{Zn} - n_bE_b - E_{str}(\Omega, n_{Zn}, n_b)}{A} + n_b\sigma \qquad \text{Equation (S8)}$$

In the Equation S8, $E_{Zn\text{-}b}$ is the total energy of the interface system, which is related to the formula units of Zn metal (n_{Zn}) and component b (n_b), the

configuration (Ω), and the interfacial area (A). E_{Zn} and E_b are the energy per formula unit for bulk Zn and specific component b, respectively. E_{str} is the strain energy induced by the lattice mismatch and σ is a constant related to the strain energy in Zn metal.

The ion-electron interaction on a well-converged k-point mesh is described by the Projector Augmented Wave (PAW) method with a cutoff energy of 400 eV. The exchange-correlation energy was calculated by the Perdew-Burke-Ernzerhof (PBE) functional in the Generalized Gradient Approximation (GGA). For optimizing the interface configuration, the lattice parameter perpendicular to the interface is relaxed and the others are fixed. The geometry was optimized by adopting conjugated gradient method with the convergence threshold of 10^{-5} eV in energy and 0.01 eV/Å in force, respectively. The structures were visualized via the combining utilization of VESTA.

Table S1: The summary of calculated interfacial energy (γ), bulk modulus (E) and Zn-dendrite suppression ability (γE) for different SEI compounds

Compounds	γ (meV/Å^2)	E (GPa)	γE (eV/Å^2• MPa)
$Zn_3(PO_4)_2$	357.72	98.88	35371.4
ZnF_2	282.17	98	27652.7
ZnO	197.16	130	25630.8
$Zn(OH)_2$	201.59	77.81	15685.7

Table S2: The fitted R_{ct} of Zn|Zn symmetric cells with different SEI components.

Samples	R_{ct} (Ω)	E_{rror} (%)
Bare Zn	290.6	5.42
$Zn_3(PO_4)_2$-Zn	288.5	1.56
ZnF_2-Zn	15.41	2.98

Table S3: The fitted R_{ct} of Zn|Zn symmetric cells with bare Zn at different temperatures

T (K)	R_{ct} (Ω)	E_{rror}/%	ln (R_{ct}^{-1}/Ω^{-1})
303.15	302.9	5.85	-5.71
308.15	180.1	3.58	-5.19
313.15	147.2	4.25	-4.99
318.15	112.3	5.56	-4.72
323.15	102.1	4.44	-4.63
328.15	83.14	3.99	-4.42
333.15	65.98	4.08	-4.19
338.15	57.92	4.30	-4.06
343.15	50.31	4.48	-3.92
348.15	25.46	4.60	-3.24
353.15	15.98	4.88	-2.77
358.15	12.54	5.13	-2.53

Table S4: The fitted R_{ct} of Zn|Zn symmetric cells with ZCS-Zn at different temperatures

T (K)	R_{ct} (Ω)	E_{rror}/%	ln (R_{ct}^{-1}/Ω^{-1})
303.15	184.2	2.29	-5.22
308.15	131.4	2.04	-4.88
313.15	96.67	2.20	-4.578
318.15	70.94	1.81	-4.268
323.15	63.63	2.01	-4.158
328.15	61.29	3.26	-4.12
333.15	52.44	3.68	-3.96
338.15	40.28	4.09	-3.70
343.15	32.6	4.47	-3.48
348.15	24.56	4.72	-3.20
353.15	19.33	4.78	-2.96
358.15	16.13	5.53	-2.78

Table S5: Corrosion potential and corrosion current density of bare Zn and ZCS-Zn

Electrode	E_{corr} (V)	J_{corr} (mA cm^{-2})	I (%)
Bare Zn	-0.989	9.79	-
ZCS-Zn	-0.982	2.22	77.3%

Inhibition efficiency (*I*) was used to evaluate the effect of in-situ ZCS on the anti-corrosion performance of Zn, which could be calculated according the following equation:

$$I = (J_{corr} - J'_{corr}) / J_{corr} \quad \text{Equation(S9)}$$

where J_{corr} and J'_{corr} are the corrosion current density of bare Zn and ZCS-Zn, respectively.

Table S6: The Tafel parameters and exchange current density of hydrogen evaluation (I_{H_2}) for bare Zn and ZCS-Zn

Electrolyte	a/mV	b/mV dec^{-1}	I_{H_2}/mA cm^{-2}
Bare Zn	-1063.88	-338.11	7.14×10^{-4}
ZCS-Zn	-1149.19	-301.31	1.53×10^{-4}

Table S7: The summary of cumulative capacity, the largest current density (j_{max}), and the largest areal capacity (C_{max}) applied to Zn in the recent reports using mildly acidic aqueous electrolytes.

No.	Electrodes	Electrolyte	j (mA cm^{-2})	C (mA h cm^{-2})	Lifespan (h)	Cumulative capacity (mA h cm^{-2})	j_{max} (mA cm^{-2})	C_{max} (mA h cm^{-2})	$j_{max}\times C_{max}$	Ref.
1	Zn-PA	2 M $ZnSO_4$	0.5	0.25	8000	2000	10	10	100	[13]
2	100TiO_2@Zn	3 M $Zn(CF_3SO_3)_2$	1	1	150	75	3	1	3	[14]
3	Zn@C	8 M $NaClO_4$+0.4 M $Zn(CF_3SO_3)_2$	2.5	1	250	312.5	10	1	10	[15]
4	NA-Zn-60	3 M $ZnSO_4$	0.25	0.05	2000	250	10	5	50	[16]
5	Zn/Cu	3 M $ZnSO_4$	1	0.5	1500	750	5	0.5	2.5	[17]
6	Zn@ZnO-3D	2 M $ZnSO_4$	5	1.25	500	1250	5	1.25	6.25	[7]
7	100Al_2O_3@Zn	3 M $Zn(SO_3CF_3)_2$	1	1	500	250	3	1	3	[18]

No.	Electrodes	Electrolyte	j (mA cm^{-2})	C (mA h cm^{-2})	Lifespan (h)	Cumulative capacity (mA h cm^{-2})	j_{max} (mA cm^{-2})	C_{max} (mA h cm^{-2})	$j_{max}\times C_{max}$	Ref.
8	In@Zn	2 M $ZnSO_4$	4	1	400	800	4	1	4	[19]
9	PVB@Zn	1 M $ZnSO_4$	0.5	0.5	2200	500	4	2	8	[3]
10	Zn-KL	2 M $ZnSO_4$+0.1 M $MnSO_4$	4.4	1.1	800	1760	4.4	1.1	4.84	[20]
11	ZnS@Zn	1 M $ZnSO_4$	2	2	1100	1100	2	2	4	[21]
12	Zn@ZnO-HPA-2.0	1 M $Zn(OTF)_2$	5	2.5	100	250	5	2.5	12.5	[22]
13	Zn-Sc_2O_3	2 M $ZnSO_4$ + 0.1 M $MnSO_4$	2	2	240	240	2	2	4	[23]
14	Zn/CNT	2 m $ZnSO_4$	2	2	200	200	20	2.5	50	[24]
15	Zn@CFs	2 M$ZnSO_4$ + 0.1 M $MnSO_4$	1	1	160	80	1	1	1	[25]

No.	Electrodes	Electrolyte	j (mA cm^{-2})	C (mA h cm^{-2})	Lifespan (h)	Cumulative capacity (mA h cm^{-2})	j_{max} (mA cm^{-2})	C_{max} (mA h cm^{-2})	$j_{max} \times C_{max}$	Ref.
16	Ti_3C_2Tx MXene@Zn	$ZnSO_4$	1	1	300	150	5	4	20	[26]
17	3D Zn	2 M $ZnSO_4$	0.5	0.5	350	87.5	1	2	2	[27]
18	Zn/Cu	1 M $ZnSO_4$+ 0.5 M Na_2SO_4 + 0.1 g/L PAM	20	1	55	1100	20	4	80	[28]
19	DCP-Zn-30	2 M $Zn(CF_3SO_3)_2$	5	10	200	500	5	10	50	[29]
20	Zn@CNT	2 M $Zn(CF_3SO_3)_2$	1	1	400	200	5	5	25	[30]
21	Zn/CNT	2 M $ZnSO_4$	3	0.5	166.67	250	3	0.5	1.5	[9]
22	Zn MS @C	1 M $ZnSO_4$ + 0.05 M H_2SO_4	2	1	425	425	2	1	2	[31]

No.	Electrodes	Electrolyte	j (mA cm^{-2})	C (mA h cm^{-2})	Lifespan (h)	Cumulative capacity (mA h cm^{-2})	j_{max} (mA cm^{-2})	C_{max} (mA h cm^{-2})	$j_{max}\times C_{max}$	Ref.
23	Zn	3 M $Zn(CF_3SO_3)_2$ + Et_2O	0.2	0.2	250	125	1	0.2	0.2	[32]
24	Zn	water@ZnMOF-808	0.1	0.05	360	18	0.1	0.05	0.005	[33]
25	Zn	LZ-DES/2H_2O	0.1	0.074	2400	120	0.5	0.5	0.25	[34]
26	Zn	ILZE	2	0.5	3000	1500	10	0.5	5	[35]
27	Zn	30M $ZnCl_2$	0.2	0.033	600	118.8	1	0.4	0.4	[36]
28	Zn	ZPSAM	2	0.5	1000	1000	2	0.5	1	[37]
29	Zn	1 M $Zn(Ac)_2$+ 0.4 M $Mn(Ac)_2$	1	1	800	400	5	1	5	[38]
30	Zn	1 M $Zn(TFSI)_2$ + 20 M LiTFSI	0.2	0.067	170	34	1	0.068	0.068	[39]

No.	Electrodes	Electrolyte	j (mA cm^{-2})	C (mA h cm^{-2})	Lifespan (h)	Cumulative capacity (mA h cm^{-2})	j_{max} (mA cm^{-2})	C_{max} (mA h cm^{-2})	$j_{max}\times C_{max}$	Ref.
Our work	ZCS-Zn	2 M $ZnSO_4$+0.05 M KPF_6	5	10	808	2020	10	20	200	-

Table S7 is divided in three parts with different colors, which represent different types of reported strategies, from top to bottom: 1) interface modification, 2) structural design, and 3) electrolyte optimization. Cumulative capacity is the summation of the capacity plated on each individual cycle prior to cell shorting or excessive impedance rise. It is a parameter that comprehensively considers both deposition capacity and cycle life, thus the comparison of cumulative capacity is more suitable to evaluate the effectiveness of various strategies than a mere comparison of cycle number or cycle time. Due to the long life (202 cycles) at a high areal capacity (10 mA h cm^{-2}), the cumulative capacity of our work could up to 2020 mA h cm^{-2}, which has reached the highest level in Zn-metal batteries built on mildly acidic aqueous electrolyte, to the best of our knowledge.

It can be found that working at the high current density of 20 mA cm^{-2} has been realized through the utilization of three-dimensional structural electrode. However, in the recent reports, no areal capacity exceeded 10 mA h cm^{-2}, no system displayed both a current density exceeding 10 mA cm^{-2} and an areal capacity exceeding 10 mA h cm^{-2}. To the best of our knowledge, the areal capacity of 20 mA h cm^{-2} in this work is the record for the so far reported Zn|Zn symmetric cells, besides, the current density applied to Zn|Zn symmetric cells could reach 10 mA cm^{-2}, demonstrating

its high probability of simultaneously meeting the requirements for practical application with high current and large capacity.

Table S8: The fitting results of R_{ct} of the Zn|MnO_2 full cells before and after 300 cycles at 5 A g^{-1}.

Sample		R_{ct} (Ω)	E_{rror}(%)
Bare Zn|MnO_2	Pristine	34.2	4.02
	300th	177	2.43
ZCS-Zn|MnO_2	Pristine	31.4	3.39
	300th	65.9	2.62

Table S9: The fitting results of R_{ct} of the Zn|AC hybrid supercapacitors after different cycles at 1 A g^{-1}.

	Sample	R_{ct} (Ω)	E_{rror}(%)
Bare Zn|AC	Pristine	29.8	6.55
	100th	112	3.52
	300th	186	2.24
ZCS-Zn|AC	Pristine	28.1	6.73
	100th	44.2	3.22
	300th	51.8	1.49

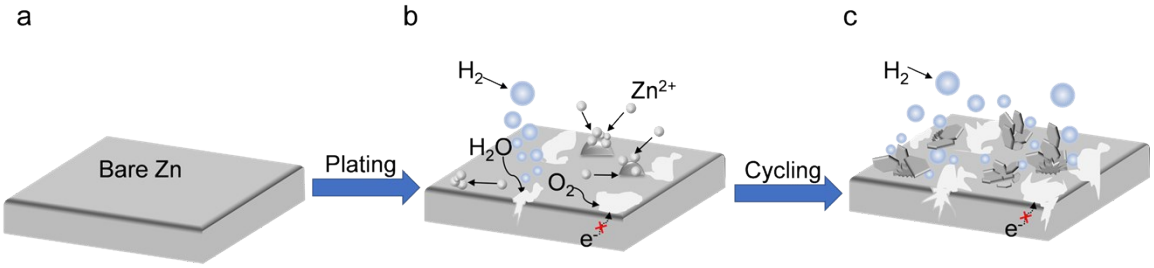

Fig. S1: Schematic illustration of the problems faced by bare Zn in aqueous electrolyte, including the dendrite growth, corrosion, passivation, and hydrogen evolution.

During the initial stage of electrodeposition, Zn^{2+} ions prefer to nucleate at the most energetic sites and aggregate to form unamiable protrusions, then the subsequent Zn^{2+} ions tend to deposit at these existing sites to minimize the surface energy (Fig. S1b). These localized protrusions grow gradually and evolve to fragile dendrites, which is likely to induce internal short-circuit and the formation of dead Zn (Fig. S1c).[40] Moreover, free water molecules and dissolved O_2 in aqueous electrolyte can easily corrode Zn anode, irreversibly converting active Zn resources to electrochemically inert byproducts, such as ZnO and $Zn_4(OH)_6SO_4 \cdot 5H_2O$ (Fig. S1b).[17, 41] These inert byproducts could further passivate the Zn anode, lead to severe polarization and partial dendrite growth. The fact that Zn dendrite with increased surface area will expose more fresh active Zn to aqueous electrolyte and further aggravate the corrosion in turn,[42] eventually results in poor reversibility, low

Coulombic efficiency and inferior cycling stability of ZIBs.

$$Zn^{2+} + 2e^{-} \rightarrow Zn \text{ (-0.76 V vs. SHE)} \qquad \text{Equation(S10)}$$

$$2H^{+} + 2e^{-} \rightarrow H_2 \text{ (0 V vs. SHE)} \qquad \text{Equation(S11)}$$

Due to the higher standard electrode potential of H_2/H^+ (equations S10 and S11), Zn^{2+} ion deposition process usually competes with adverse hydrogen evolution reaction (HER) during long-term cycling (Fig. S1c), further intensifying the accumulation of inert components by providing more OH^- ions around anode interface and resulting in the swelling of sealed batteries due to the rampant release of H_2.[43]

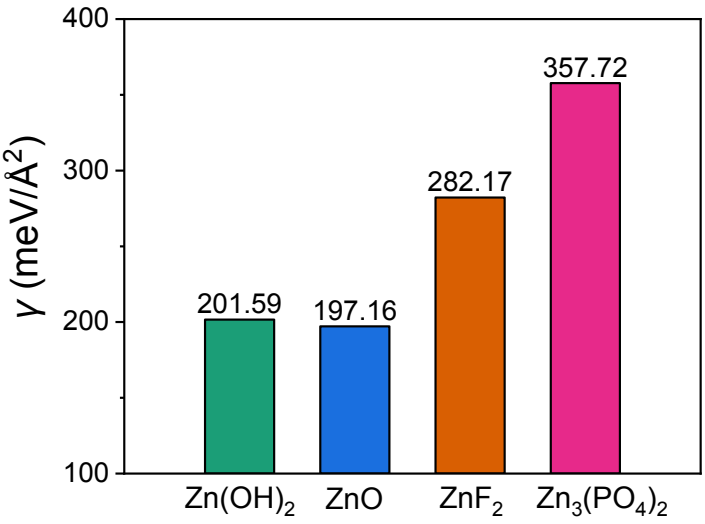

Fig. S2: The calculated interface energy γ of various SEI components.

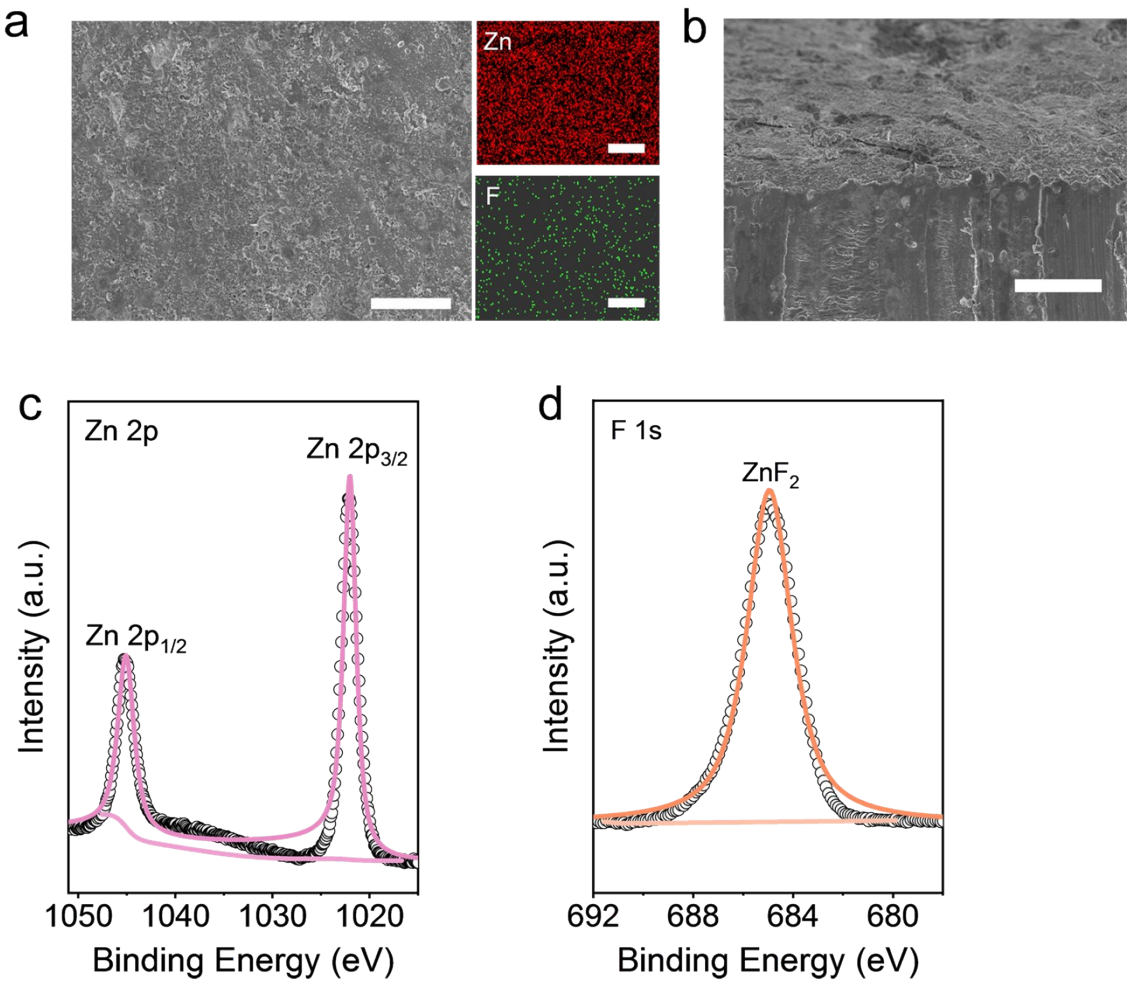

Fig. S3: Characterizations for ZnF_2-Zn. (a) SEM images and corresponding elements distribution. The scale bar is 5 μm. (b) Cross-sectional SEM image. The scale bar is 5 μm. High-resolution XPS spectra of (c) Zn 2p and (d) F 1s.

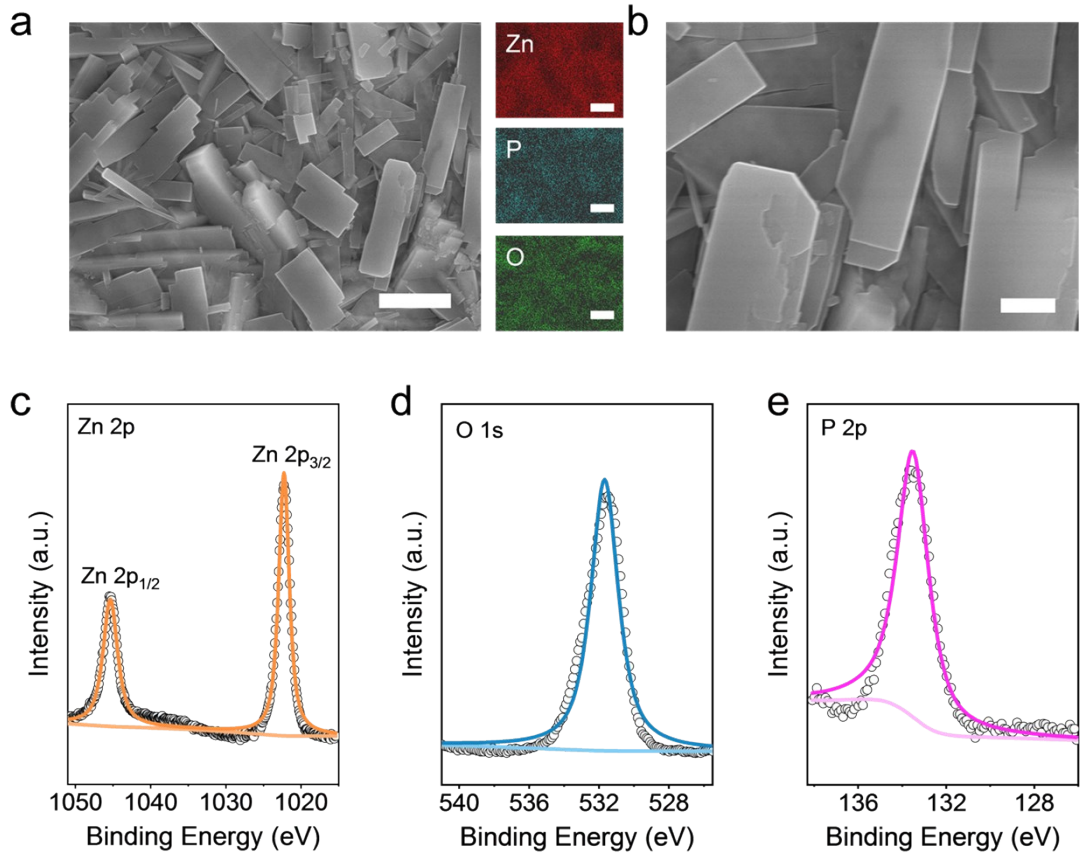

Fig. S4: Characterizations for $Zn_3(PO_4)_2$-Zn. (a) SEM images and corresponding elements distribution. The scale bars are 2 μm. (b) Enlarged SEM image. The scale bar is 500 nm. High-resolution XPS spectra of (c) Zn 2p, (d) O 1s, and (e) P 2p.

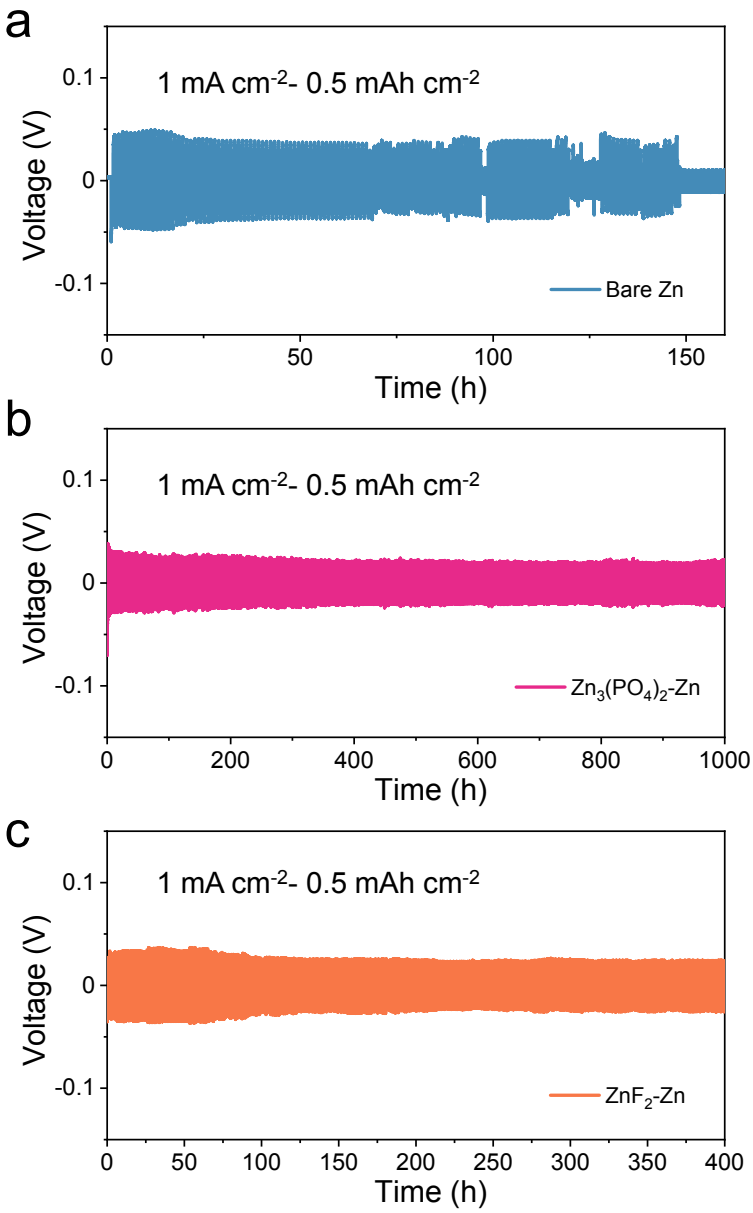

Fig. S5: Galvanostatic cycling performance of symmetric Zn|Zn cells using (a) bare Zn, (b) $Zn_3(PO_4)_2$-Zn, and (c) ZnF_2-Zn at a current density of 1 mA cm^{-2} and an areal capacity of 0.5 mA h cm^{-2}.

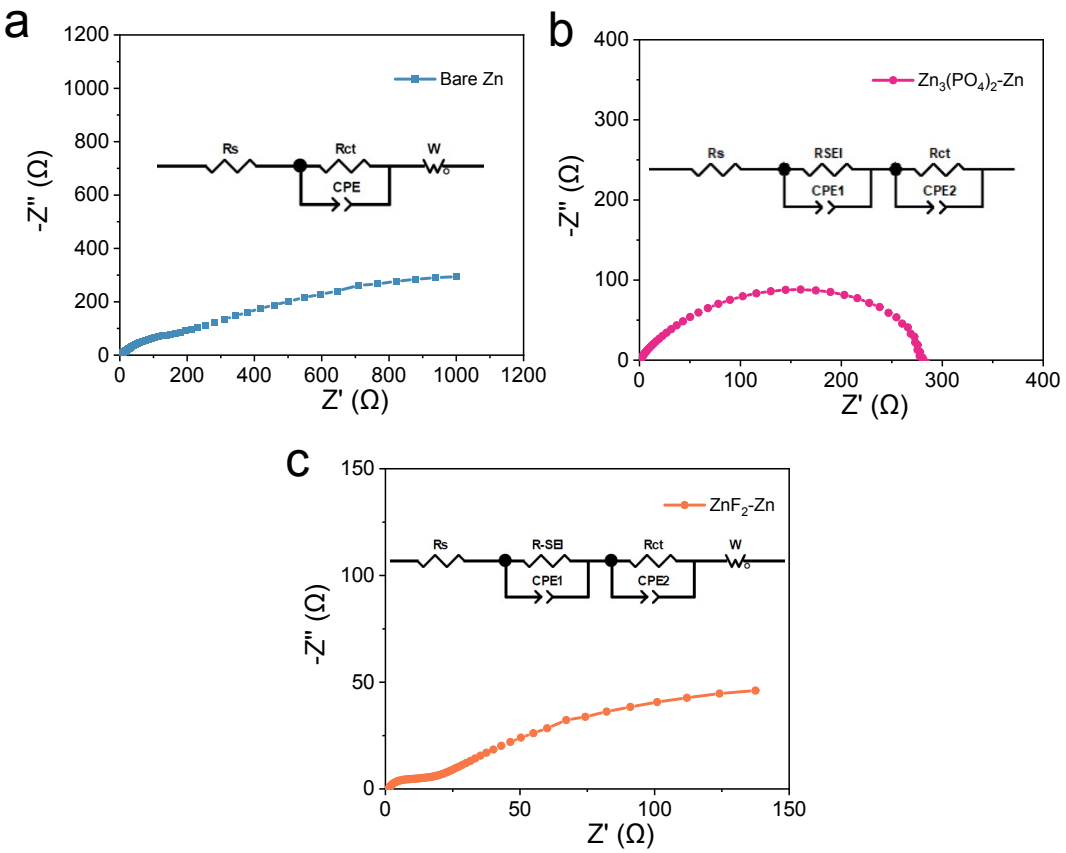

Fig. S6: EIS curves and their equivalent circuits for symmetric Zn|Zn cells using (a) bare Zn, (b) $Zn_3(PO_4)_2$-Zn, and (c) ZnF_2-Zn. In the equivalent circuit, R_s is the intrinsic resistance, *R*-SEI and the CPE in parallel with it are the interface resistance and its related double-layer capacitance. R_{ct} and the CPE in parallel with it are the charge transfer resistance and its related double-layer capacitance, respectively, and *W* represents the Warburg impedance. The fitted R_{ct} and relative standard error (E_{rror}) is also provided in Table S2. All of the fitted R_{ct} are controlled at an acceptable E_{rror} (less than 10%)

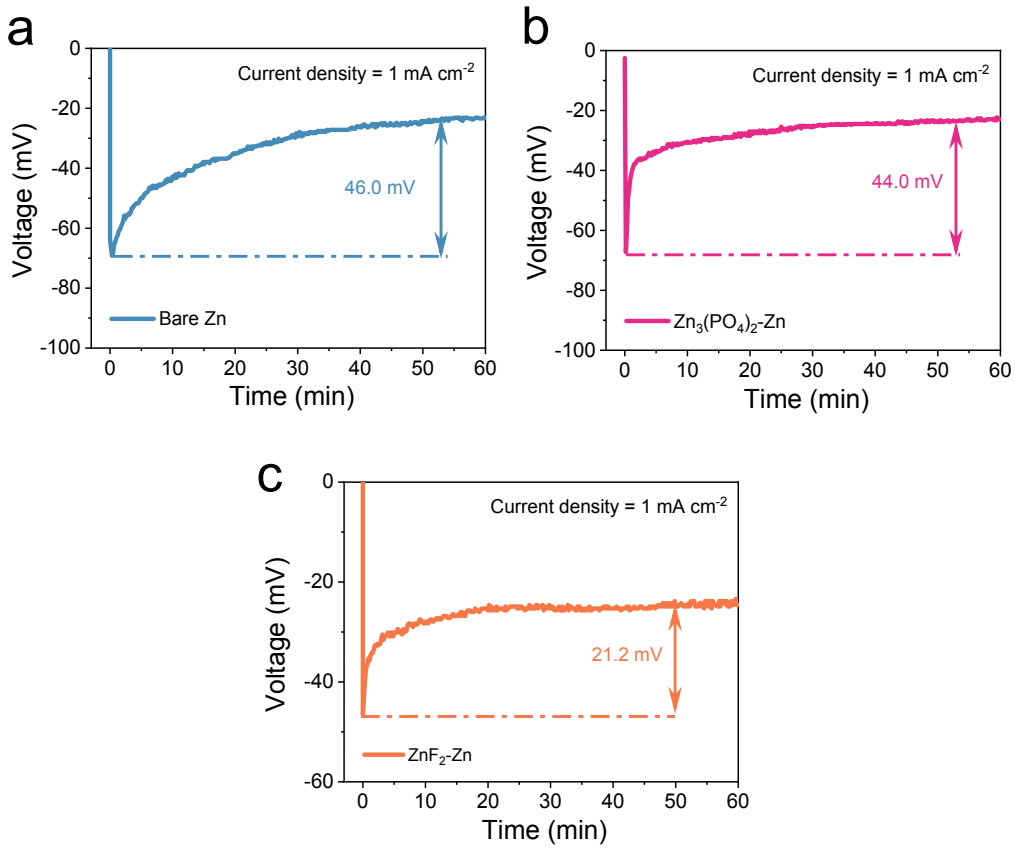

Fig. S7: Nucleation overpotential of symmetric Zn|Zn cells using (a) bare Zn, (b) $Zn_3(PO_4)_2$-Zn, and (c) ZnF_2-Zn.

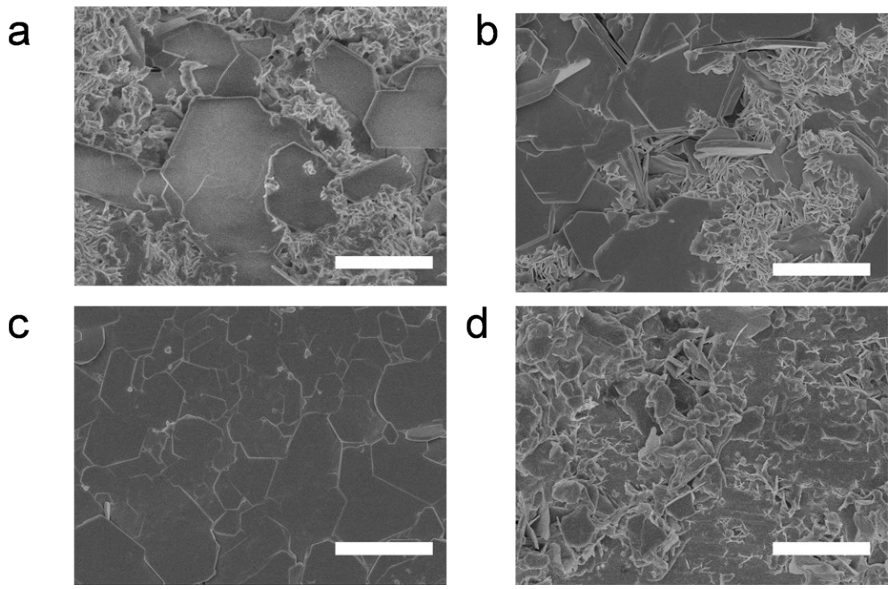

Fig. S8: The surface morphologies of the Zn deposition on Ti foil (1.13 cm^2) at 1 mA for 50 h in the (a) 2 M $ZnSO_4$ electrolyte, (b) 2 M $ZnSO_4$ electrolyte with 0.01 M KPF_6 additive, (c) 2 M $ZnSO_4$ electrolyte with 0.05 M KPF_6 additive and (d) 2 M $ZnSO_4$ electrolyte with 0.1 M KPF_6 additive. Scale bar: 10 μm.

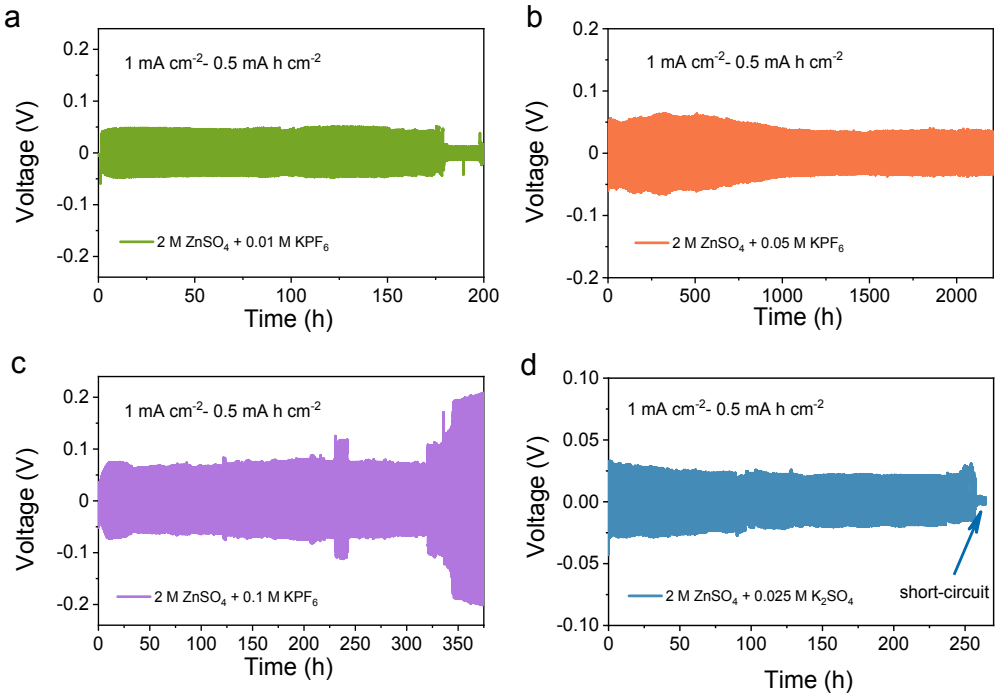

Fig. S9: Long-term galvanostatic cycling of symmetrical Zn cells in (a) 2 M $ZnSO_4$ + 0.01 M KPF_6, (b) 2 M $ZnSO_4$ + 0.05 M KPF_6, (c) 2 M $ZnSO_4$ + 0.1 M KPF_6, (d) 2 M $ZnSO_4$ + 0.025 M K_2SO_4.

It should be pointed out that the presence of K^+ ions may also promote the smooth deposition of Zn^{2+} ions via self-healing electrostatic shield mechanism.[44] However, from the fact that the lifespan of Zn|Zn symmetric cells just obtained slight improvement with the cooperation of 0.025 M K_2SO_4 additive (Fig. S9d), it can be inferred that the contribution to Zn anode performance stemming from the self-healing electrostatic shield mechanism is negligible in comparison with the effect of ZCS layer.

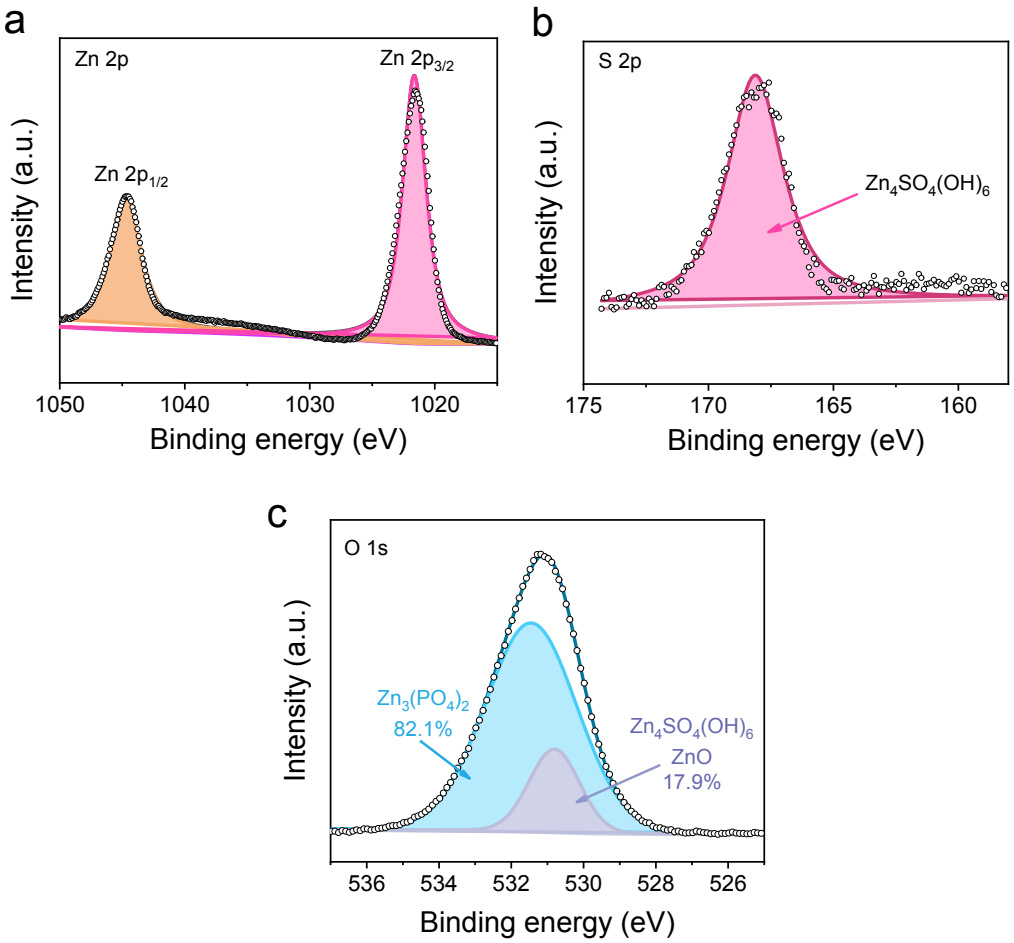

Fig. S10: XPS spectra for (a) Zn 2p, (b) S 2p and (c) O 1s of Zn anodes rested for 48 h in aqueous Zn|Zn symmetric cells with 0.05 M KPF_6.

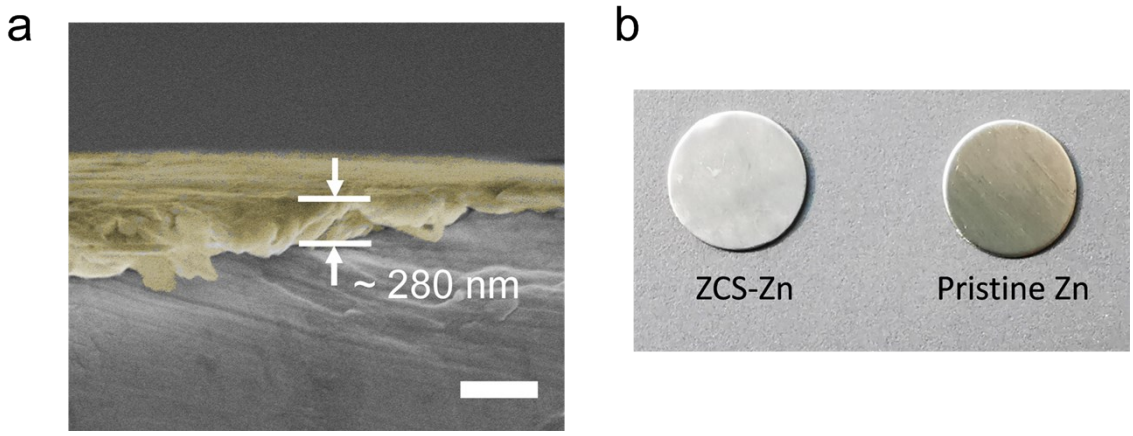

Fig. S11: (a) Cross-sectional SEM image of Zn anode after being rested for 48 h in Zn|Zn symmetric cell with 0.05 M KPF_6. Scale bar: 500 nm. (b) Photographs of Zn anode after being immersed in the electrolyte with 0.05 M KPF_6 for 48 h and pristine Zn, respectively. The diameter of Zn foil is 12 mm.

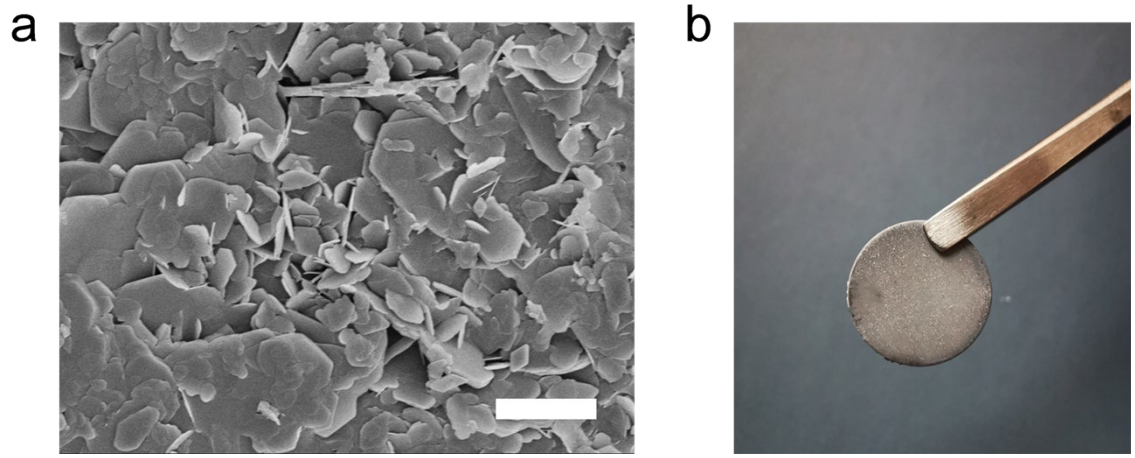

Fig. S12: (a) SEM image of Zn anode after being rested in symmetrical Zn cell with 2 M $ZnSO_4$ for 48 h. Scale bar: 2 μm. (b) Photograph of Zn anode after being immersed in 2 M $ZnSO_4$ for 48 h. The diameter of Zn foil is 12 mm.

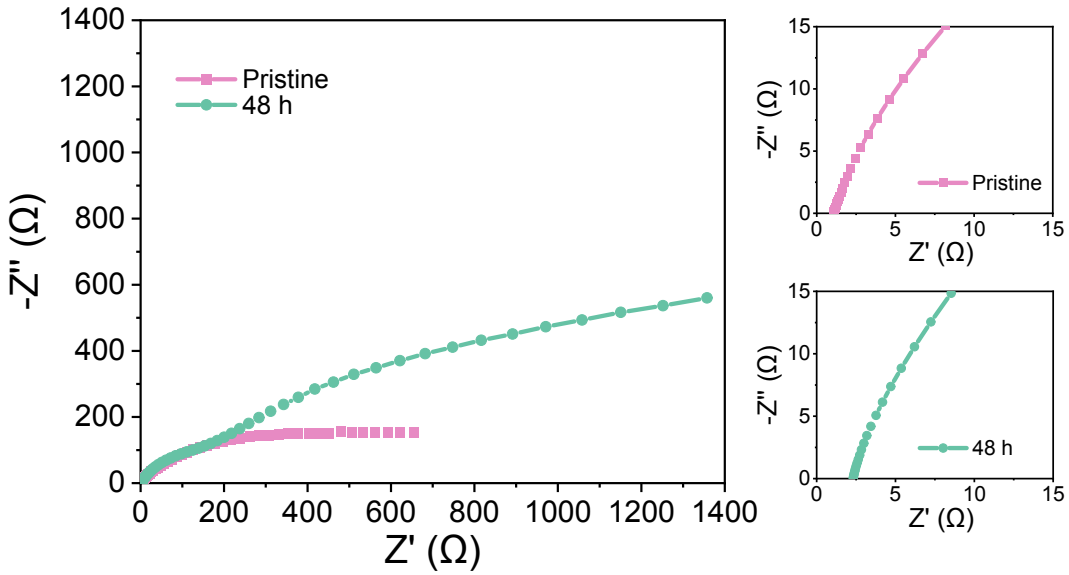

Fig. S13: EIS plots of the Zn|Zn cells using bare Zn at different standing time.

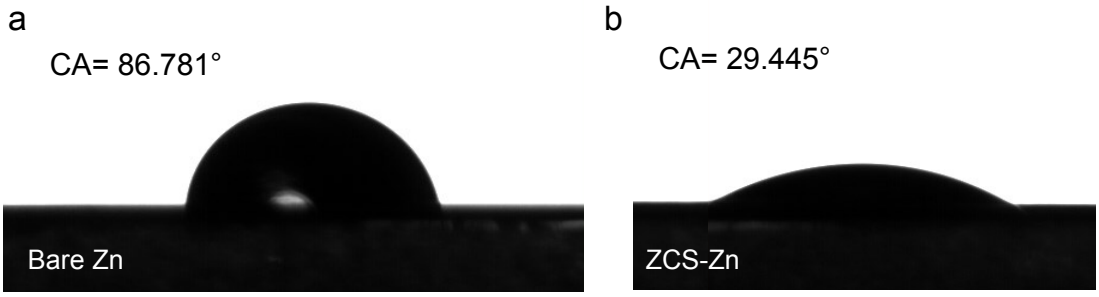

Fig. S14: Contact angles of 2 M $ZnSO_4$ electrolyte toward (a) bare Zn and (b) ZCS-Zn.

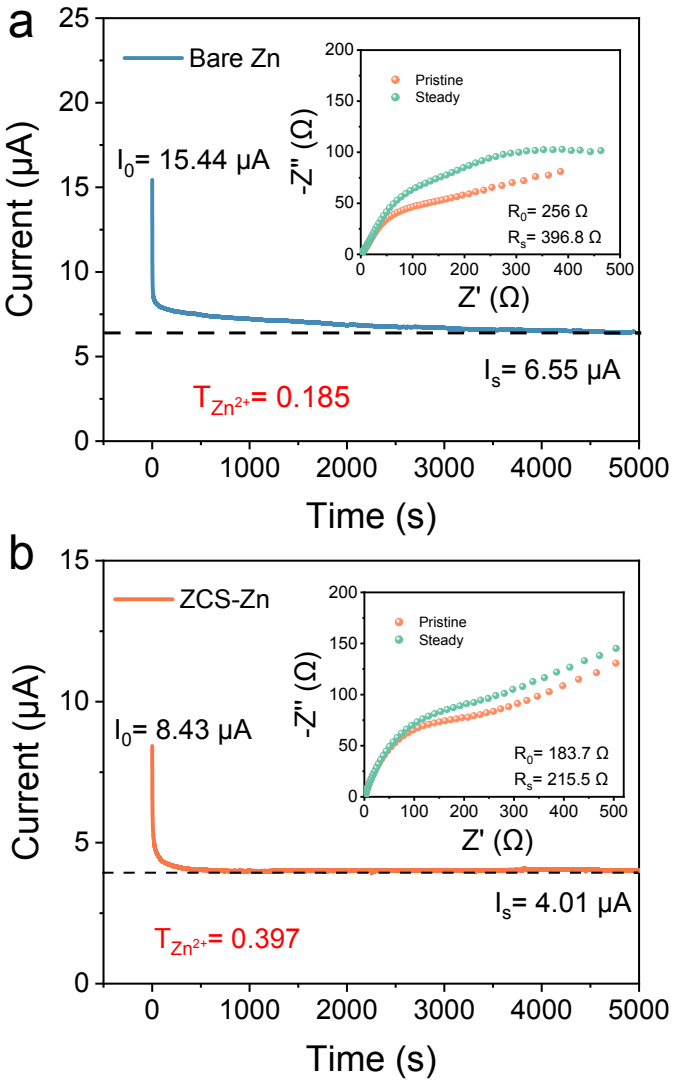

Fig. S15: Current-time curves with a constant voltage polarization of 5 mV and the insets show the impedance spectra before and after polarization. (a) bare Zn, (b) ZCS-Zn.

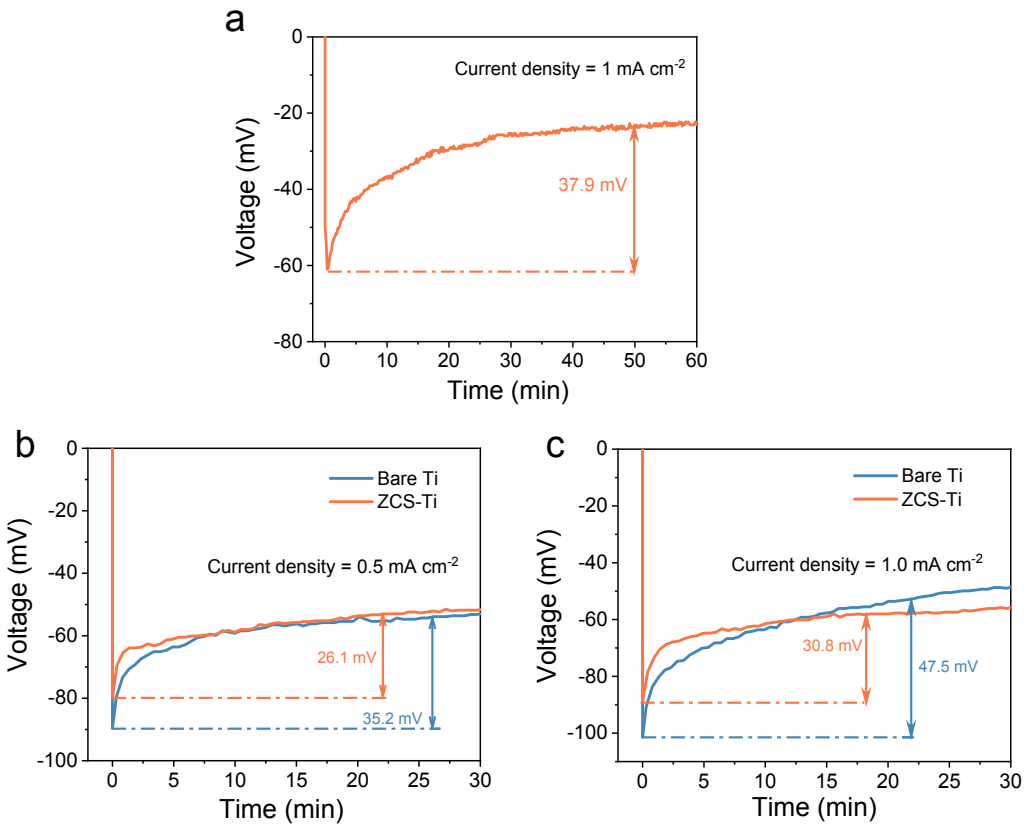

Fig. S16: Nucleation overpotential of Zn on (a) ZCS-Zn substrate at a current density of 1 mA cm^{-2}, (b) Ti substrate coated with ZCS (ZCS-Ti) and bare Ti substrate at a current density of 0.5 mA cm^{-2}, and (c) ZCS-Ti and bare Ti substrate at a current density of 1 mA cm^{-2}.

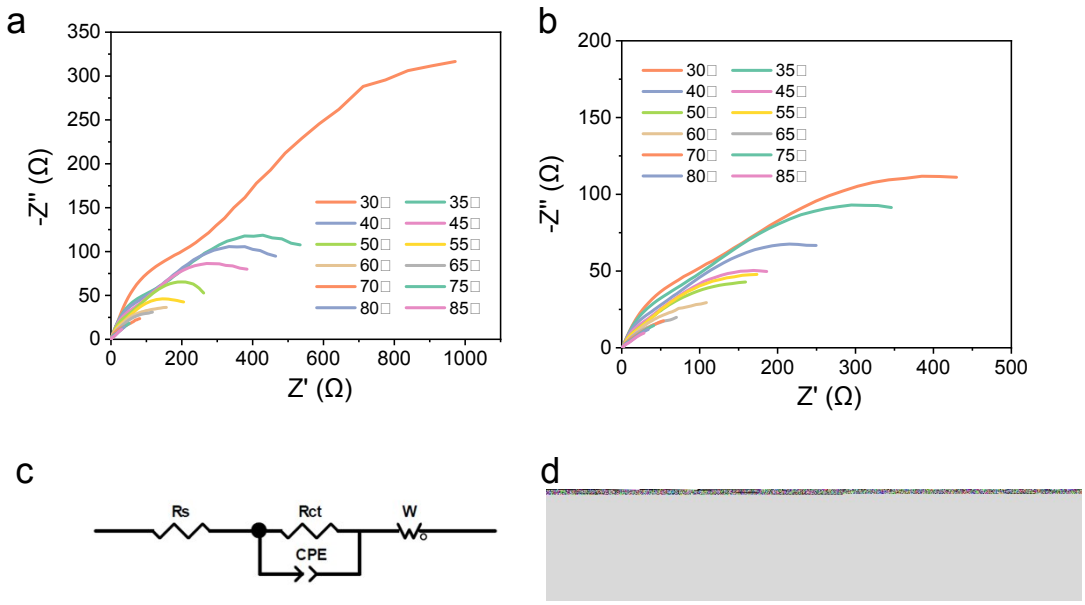

Fig. S17: (a, c) The EIS profiles at different temperatures of symmetrical Zn cell with bare Zn and the corresponding equivalent circuit used to fit the EIS curves. (b, d) The EIS profiles at different temperatures of symmetrical Zn cell with ZCS-Zn and the corresponding equivalent circuit used to fit the EIS curves.

In the equivalent circuit, R_s represents the intrinsic resistance, R_{ct} and the CPE in parallel with it are the charge transfer resistance and its related double-layer capacitance, *R*-SEI and the CPE in parallel with it are the interface resistance and its related double-layer capacitance, and *W* represents the Warburg impedance.

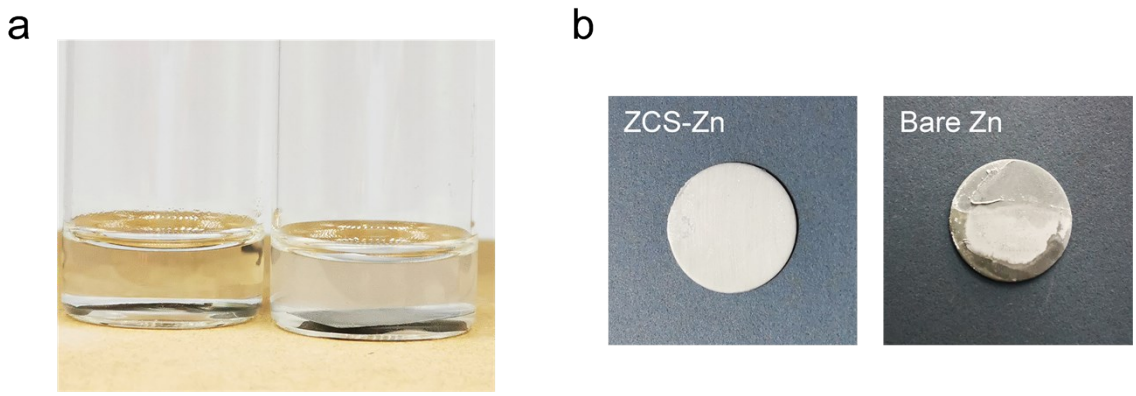

Fig. S18: (a) Photographs of the electrolytes after soaking Zn plate for 10 days. The left is 2 M $ZnSO_4$ with 0.05 M KPF_6 additive and the right is 2 M $ZnSO_4$. (b) Photographs of Zn foils after being immersed in electrolytes. The diameter of Zn foil is 12 mm.

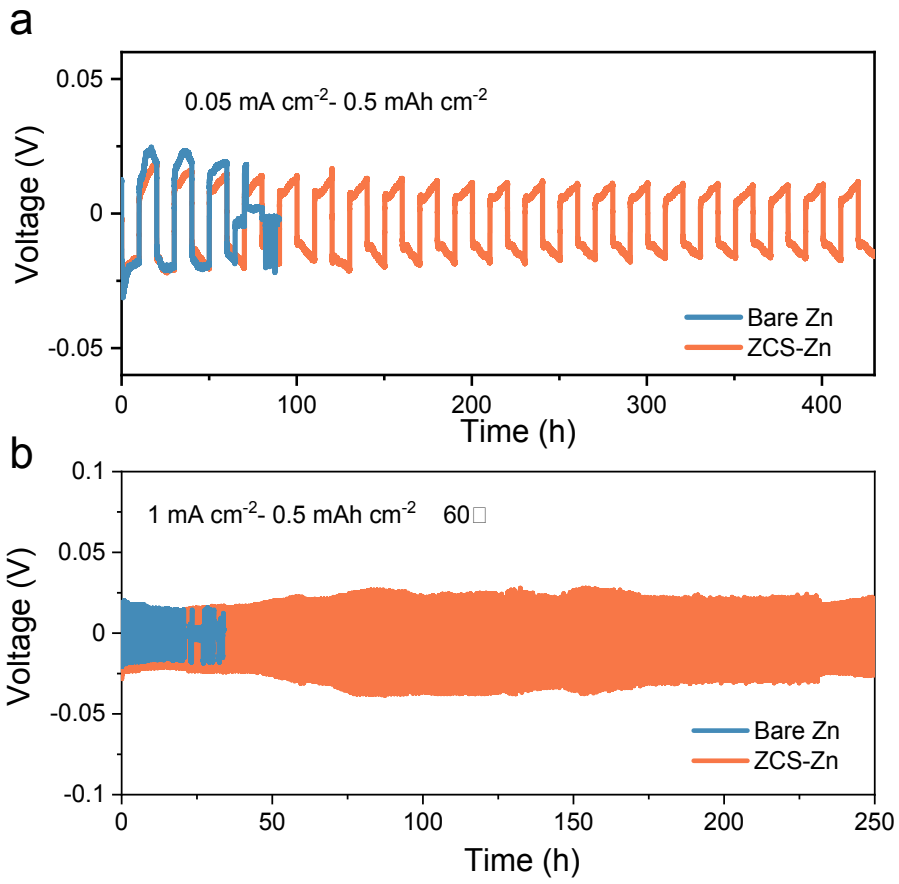

Fig. S19: Long-term galvanostatic cycling of Zn|Zn symmetrical cells with bare Zn and ZCS-Zn (a) working at the current density of 0.05 mA cm^{-2} and the areal capacity of 0.5 mA h cm^{-2}, (b) working at 60℃ with the current density of 1 mA cm^{-2} and the areal capacity of 0.5 mA h cm^{-2}.

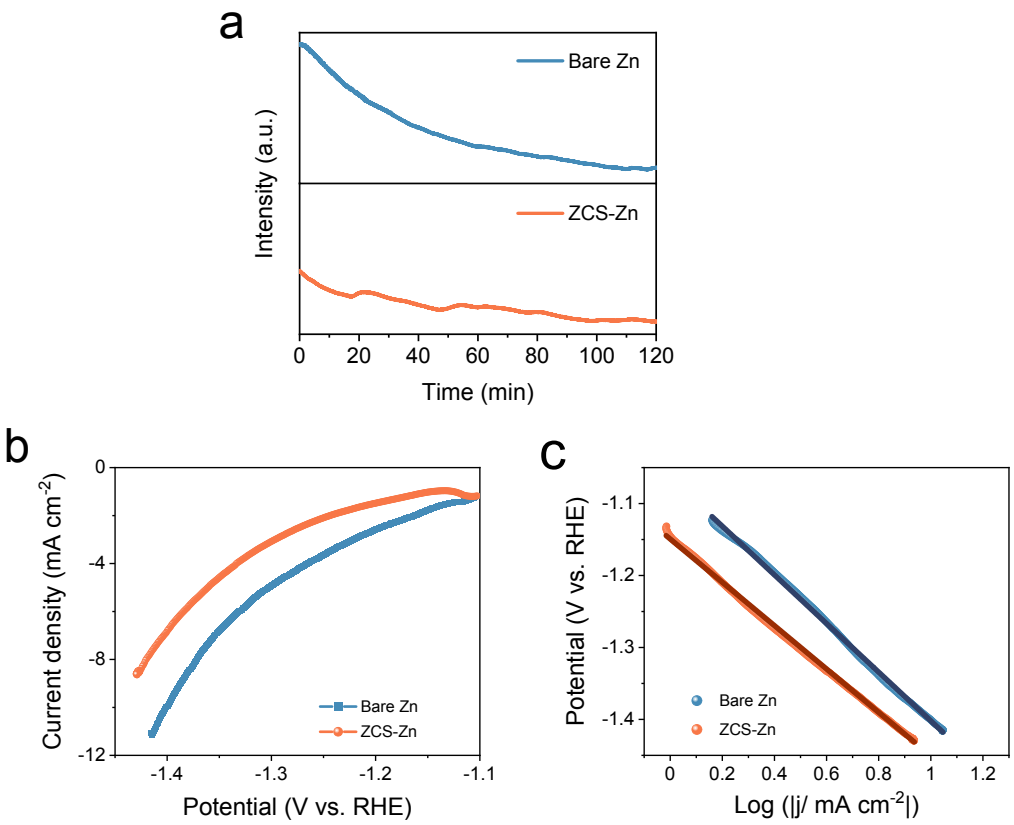

Fig. S20: (a) DEMS for Zn|Zn cells with bare Zn and ZCS-Zn at open-circuit voltage. (b) Linear sweep voltammetry (LSV) and (c) corresponding Tafel curves of bare Zn and ZCS-Zn at a scan rate of 5 mV s^{-1} in 1.0 M Na_2SO_4 solution.

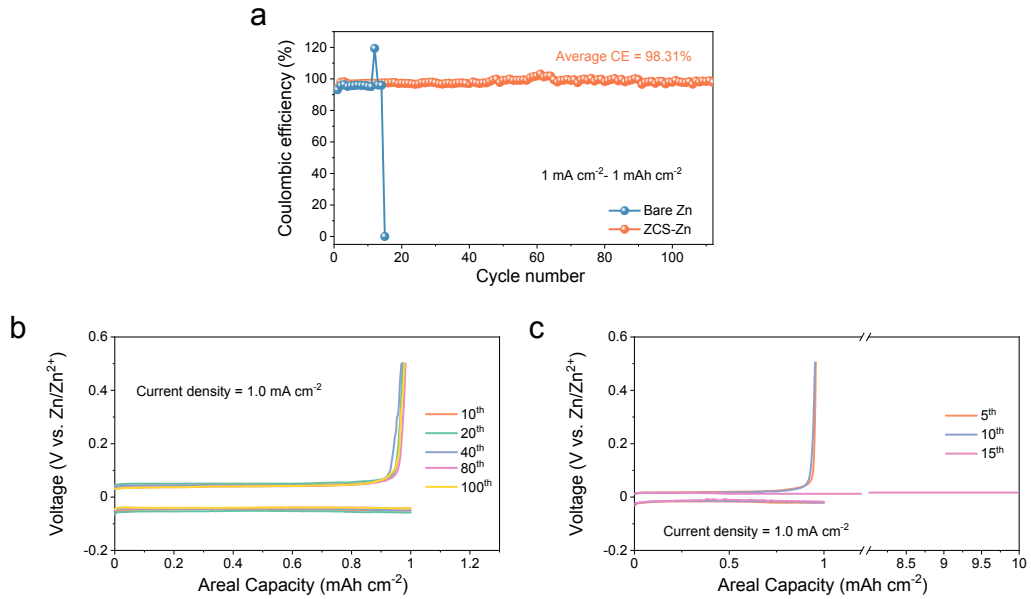

Fig. S21: (a) Coulombic efficiency and (b, c) corresponding discharge-charge profiles of Zn|Ti cells with and without ZCS. Zn was plated for 1 h at each cycle under the current density of 1 mA cm^{-2} and the stripping upper voltage was 0.5 V.

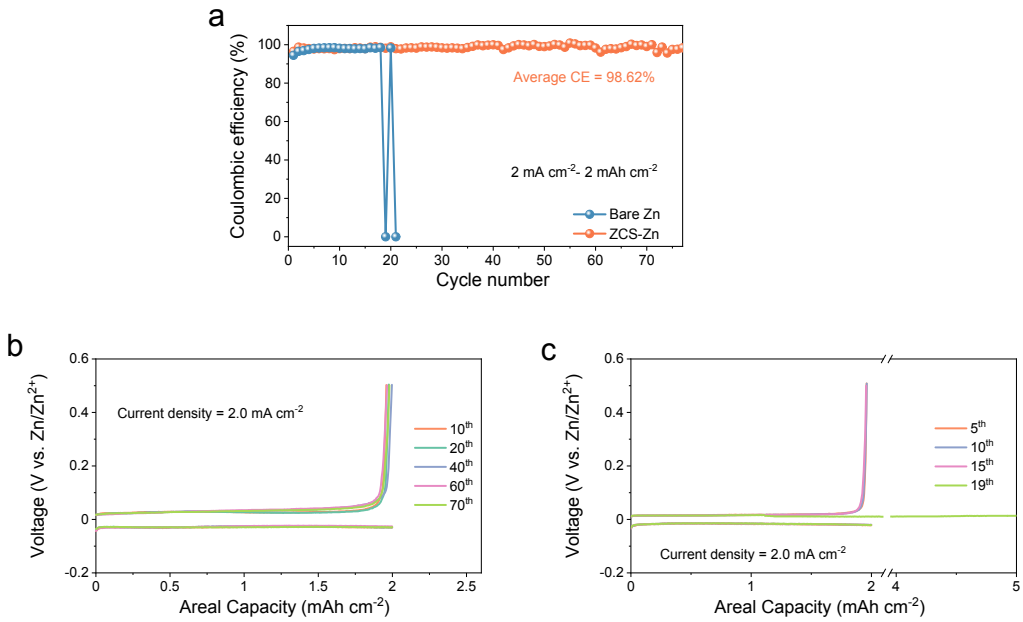

Fig. S22: (a) Coulombic efficiency and (b, c) corresponding discharge-charge profiles of Zn|Ti cells with and without ZCS. Zn was plated for 1 h at each cycle under the current density of 2 mA cm^{-2} and the stripping upper voltage was 0.5 V.

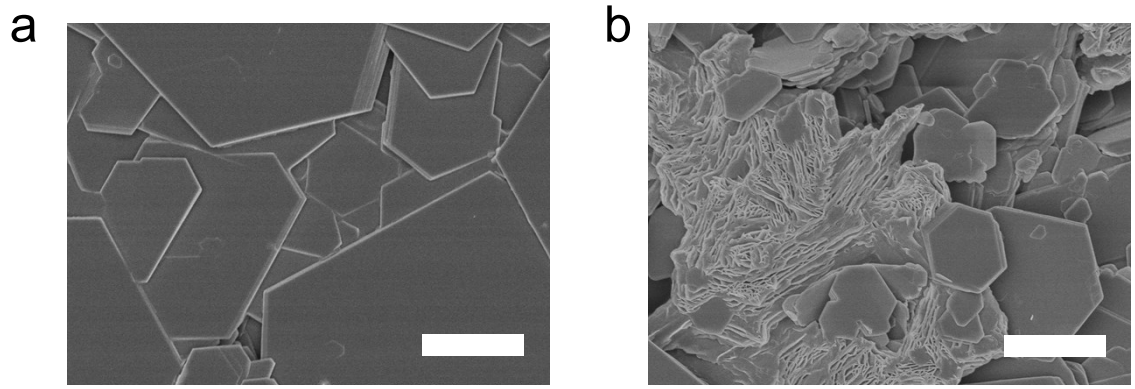

Fig. S23: The morphology of Zn deposition on the cycled Ti. (a) ZCS-Ti, (b) bare Ti.

Zn|Ti half cells were tested at the current density of 1 mA cm^{-2} with an areal capacity of 1 mA h cm^{-2} for 10 cycles and then the Zn plating morphology on Ti was investigated by SEM. It turns out that uneven Zn fragments and dendrites cover the surface of Ti without ZCS. In contrast, the Zn deposition on the ZCS-Ti display smooth and uniform morphology.

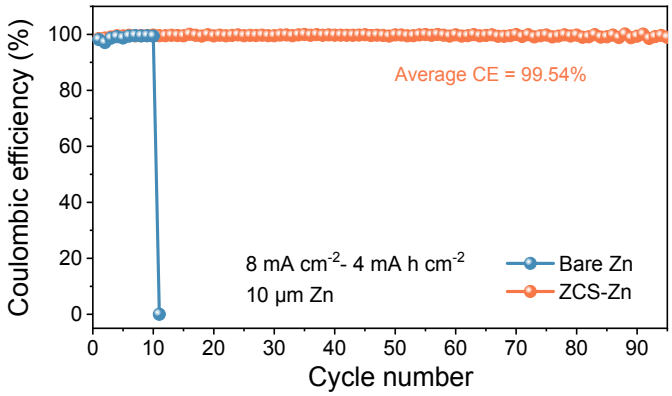

Fig. S24: CE of Zn|Ti cells with and without ZCS. Zn was plated for 0.5 h at each cycle under the current density of 8 mA cm^{-2} and the stripping upper voltage was 0.5 V. The thickness of Zn is controlled at 10 μm.

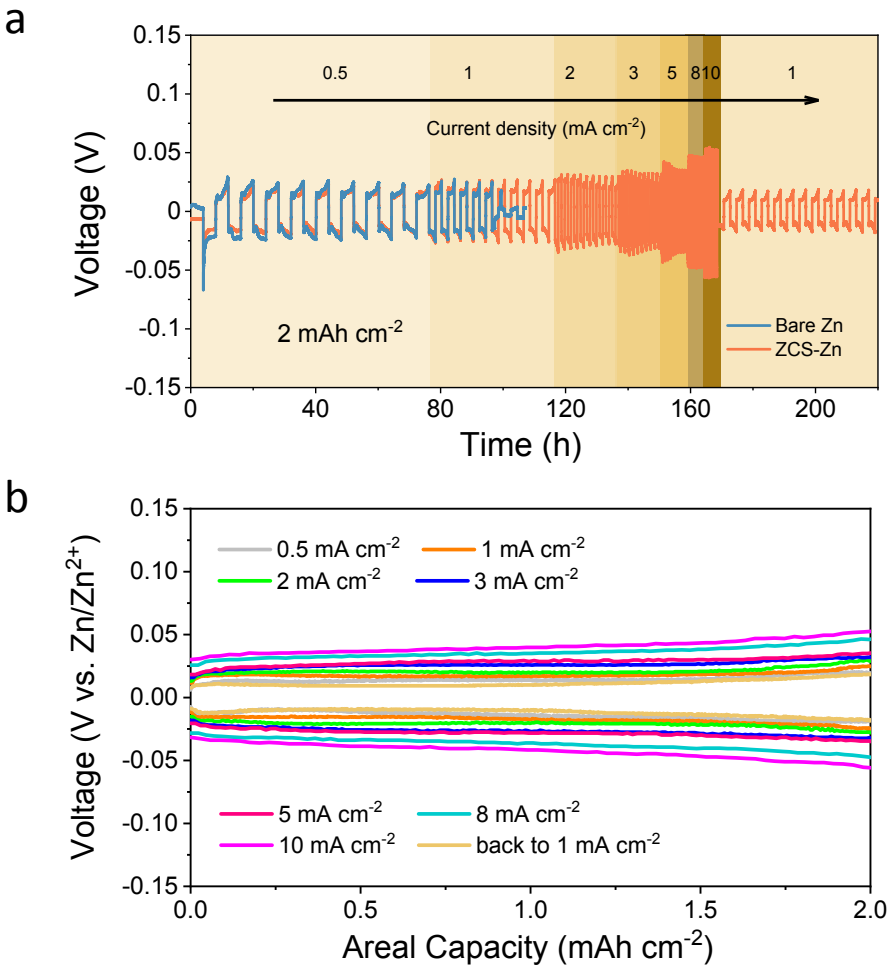

Fig. S25: (a) Rate performance of Zn|Zn cells with bare Zn and ZCS-Zn, (b) The voltage profiles of Zn|Zn cells using ZCS-Zn at different current densities.

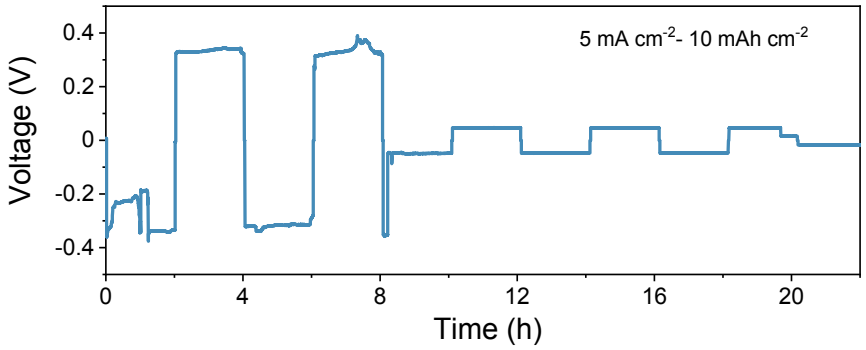

Fig. S26: The voltage profiles of Zn|Zn cells using bare Zn at a current density of 5 mA cm^{-2} and an areal capacity of 10 mA h cm^{-2}.

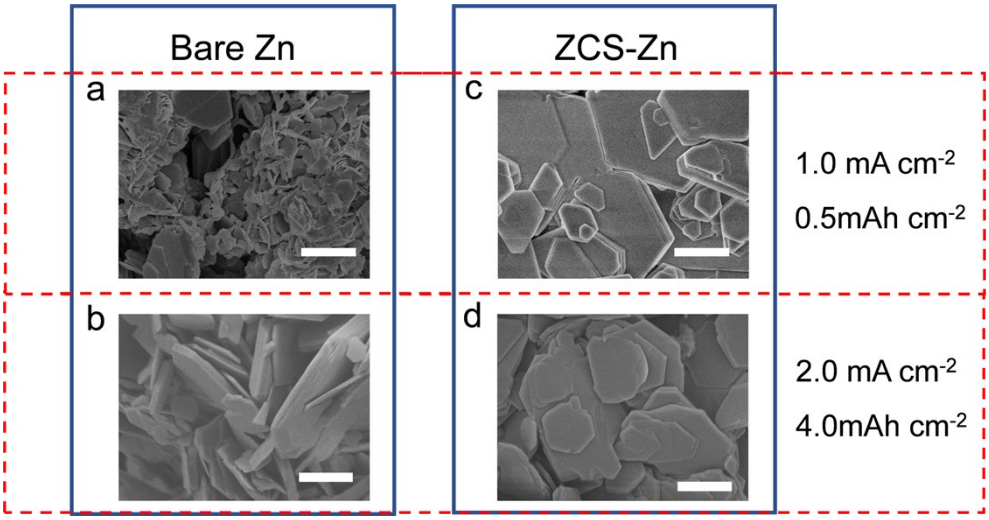

Fig. S27: SEM images of Zn anodes with or without ZCS after cycling for 100 h at different working conditions. Scale bars are 2 μm.

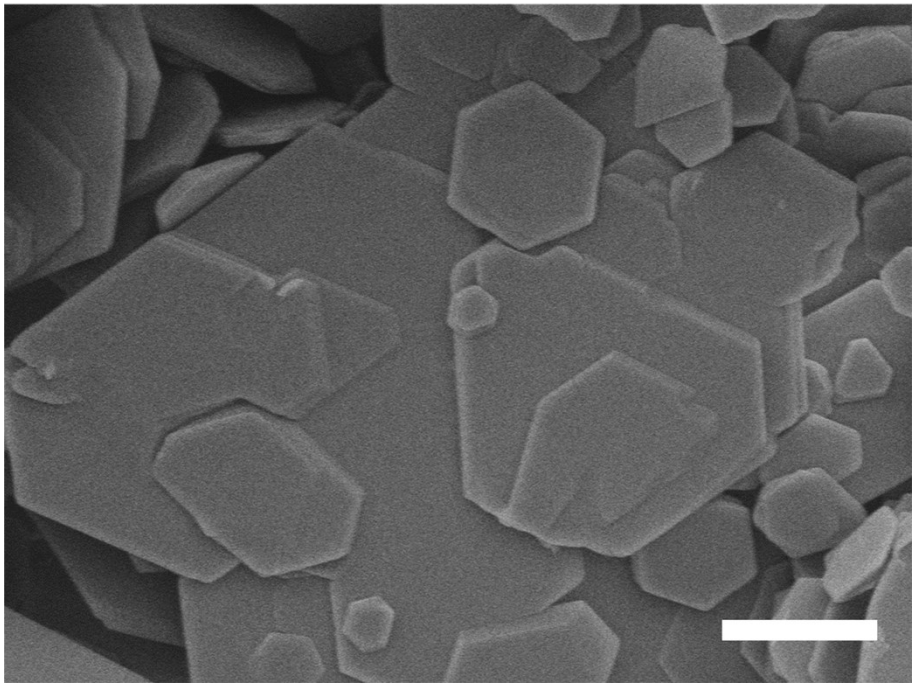

Fig. S28: SEM images of ZCS-Zn after cycling for 100 h at the current density of 5 mA cm^{-2} and the areal capacity of 10 mA h cm^{-2}. Scale bar: 2 μm.

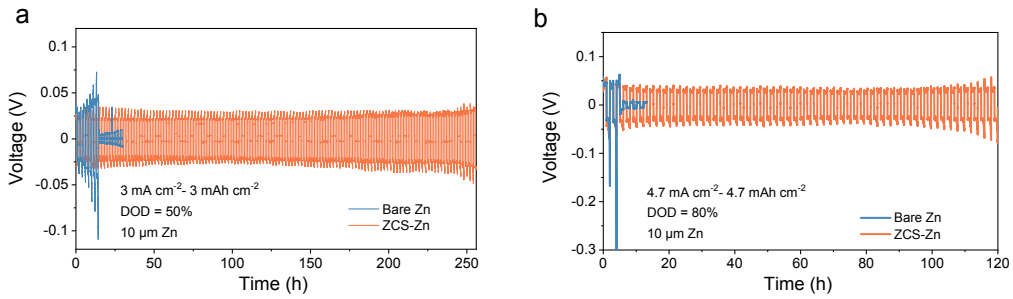

Fig. S29: Long-term galvanostatic cycling of symmetrical Zn cells using limited Zn at a high DOD. (a) 3 mA cm^{-2} -3 mA h cm^{-2}, DOD = 50%. (b) 4.7 mA cm^{-2} -4.7 mA h cm^{-2}, DOD = 80%.

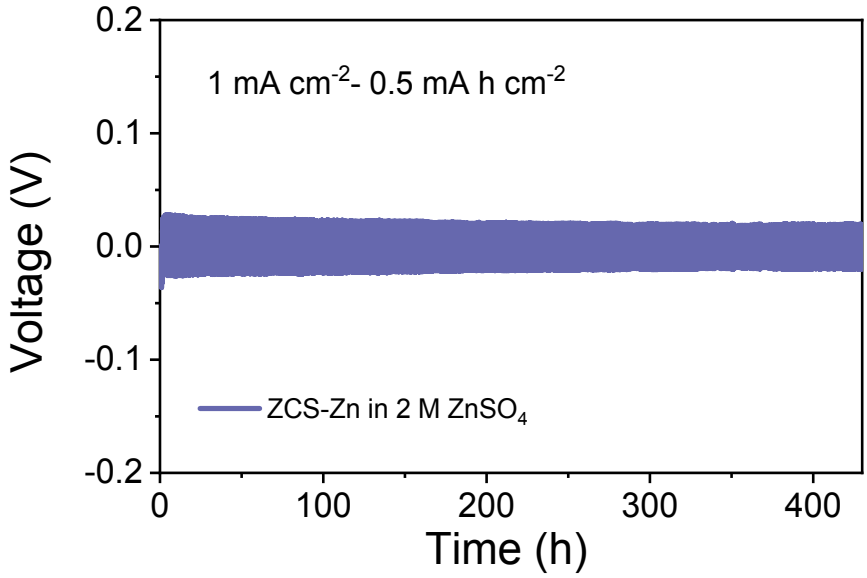

Fig. S30: Long-term galvanostatic cycling of symmetrical Zn cells with ZCS-Zn in 2 M $ZnSO_4$ electrolyte.

The ZCS-Zn electrodes fetched from Zn|Zn symmetric cells with 0.05 M KPF_6 additive have been rested for 48 h before use, then reassembled into Zn|Zn symmetric cells with 2 M $ZnSO_4$ electrolyte. Interestingly, compared with bare Zn, the ZCS-Zn anode exhibits extended cycling life over 400 h at 1 mA cm^{-2}.

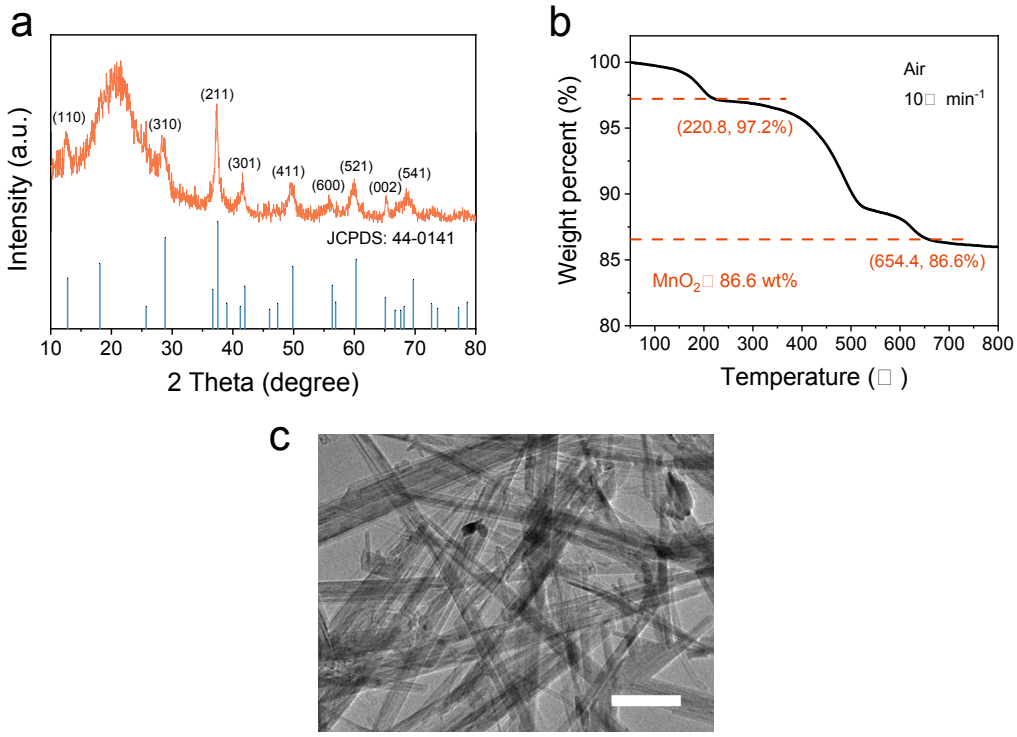

Fig. S31: Characterizations for α-MnO_2/CNT. (a) XRD pattern, (b) TGA curve, and (c) TEM image. Scale bar: 100 nm.

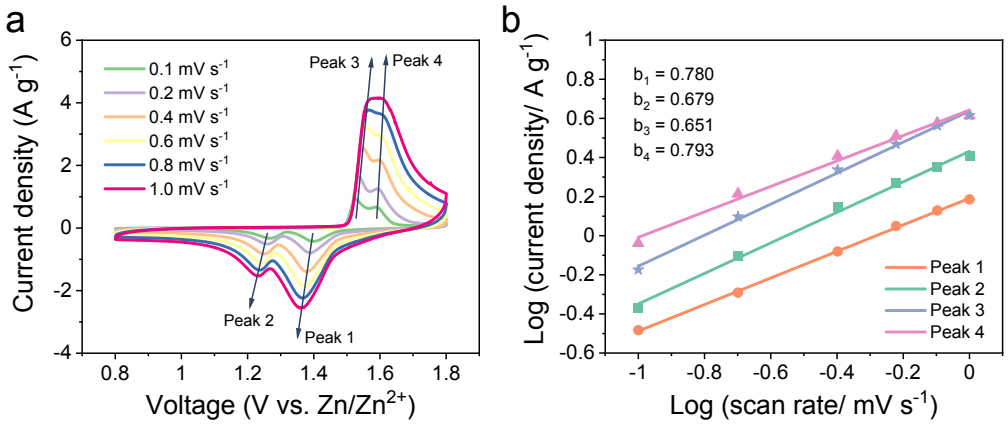

Fig. S32: (a) Cyclic voltammetry (CV) curves at different scan rates for Zn|MnO_2 cells with bare Zn. (b) The fitted lines of log (peak current density) versus log (scan rate) plots for different peaks.

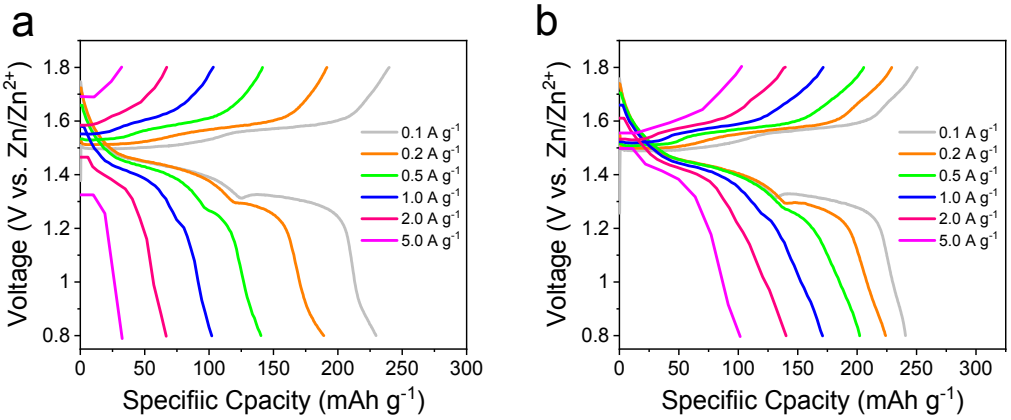

Fig. S33: GCD curves of Zn|MnO_2 cells at different current densities. (a) Zn|MnO_2 cells with bare Zn, (b) Zn|MnO_2 cells with ZCS-Zn.

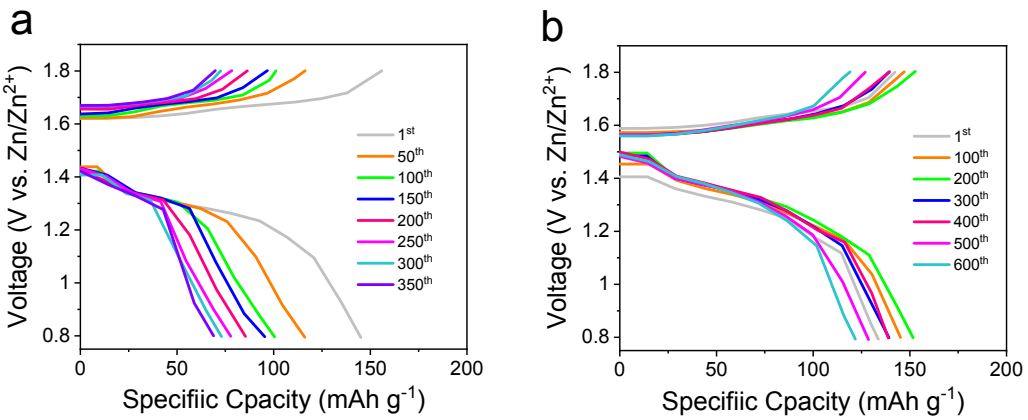

Fig. S34: GCD curves of Zn|MnO_2 cells at different cycle numbers. (a) Zn|MnO_2 cells with bare Zn, (b) Zn|MnO_2 cells with ZCS-Zn.

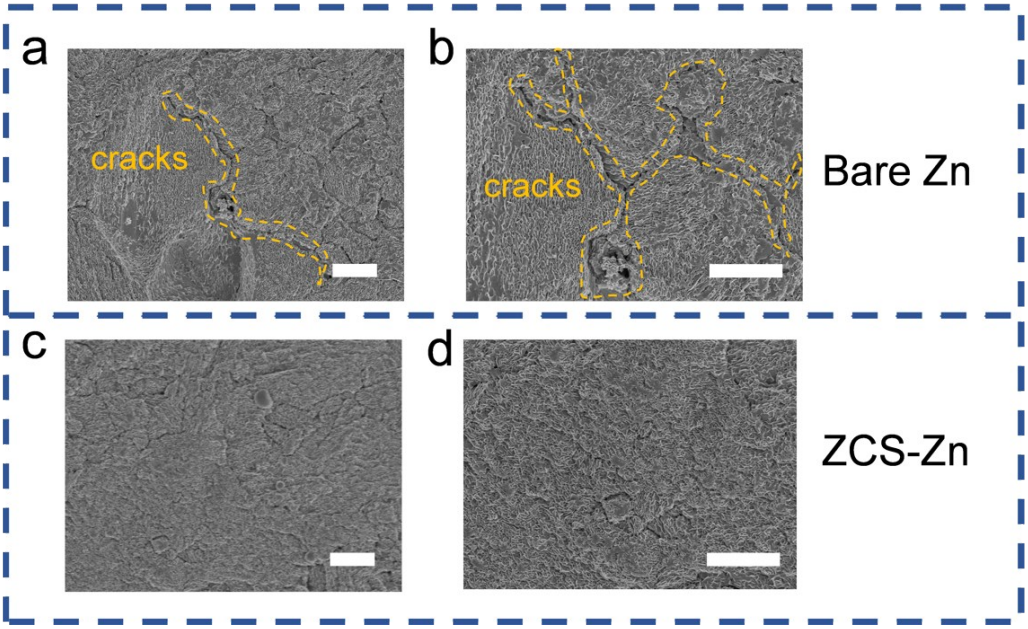

Fig. S35: SEM images of Zn anode in Zn|MnO_2 full cells after 300 cycles at 5 A g^{-1}. (a, b) Bare Zn, and (c, d) ZCS-Zn. Scale bar: 5 μm.

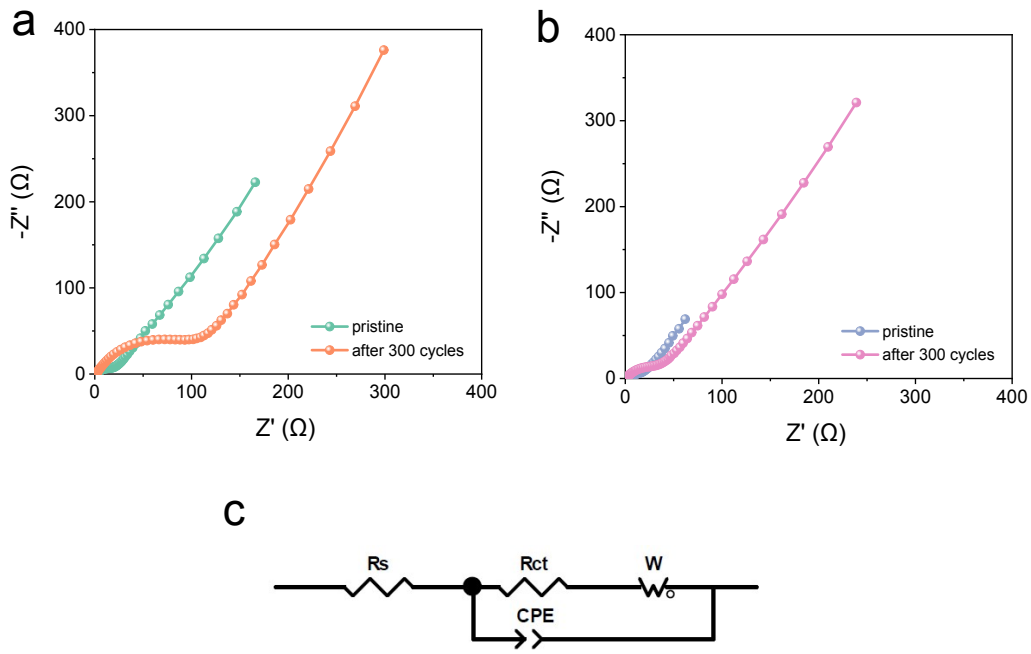

Fig. S36: EIS plots of Zn|MnO_2 cells before and after 300 cycles at 5 A g^{-1}. (a) Zn|MnO_2 cells with bare Zn, (b) Zn|MnO_2 cells with ZCS-Zn. (c) The equivalent circuit used to fit the EIS curves, which consiste of equivalent series resistance (R_s), double-layer capacitance (CPE), charge transfer resistance (R_{ct}) and Warburg resistance (W).

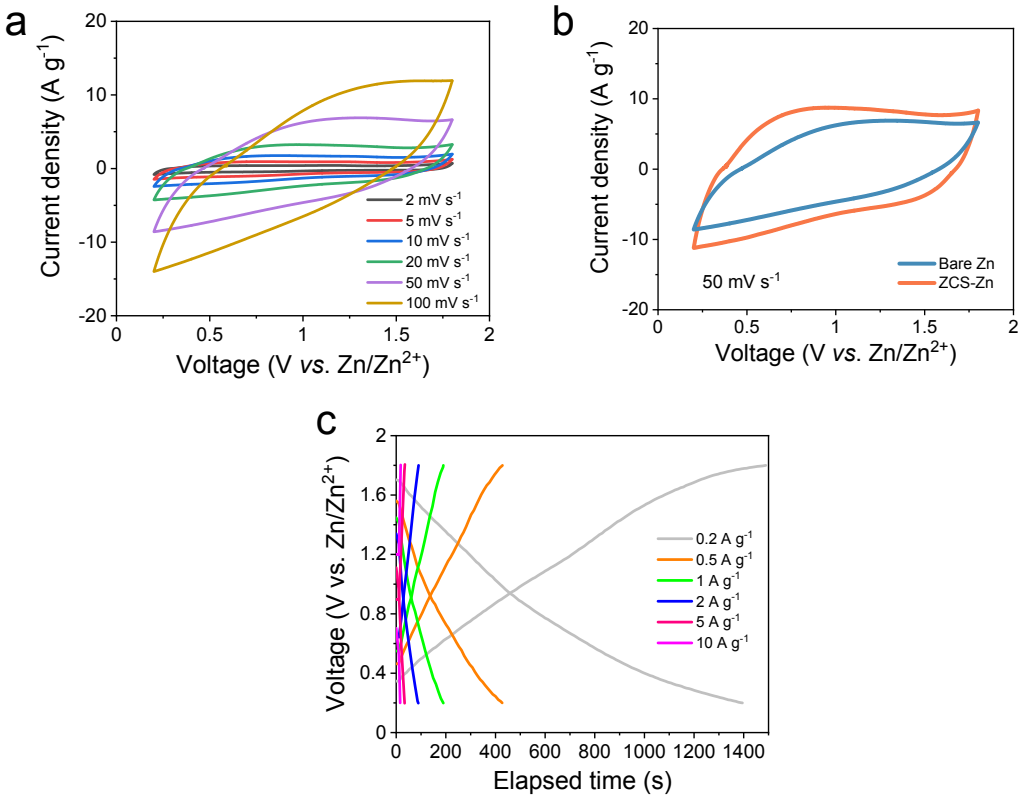

Fig. S37: (a) CV curves of Zn|AC ZHC using bare Zn at different scan rates from 2 mV s^{-1} to 100 mV s^{-1}. (b) The comparison of CV curves for Zn|AC ZHCs using bare Zn and ZCS-Zn at 50 mV s^{-1}. (c) GCD plots of Zn|AC ZHC using bare Zn at different current densities from 0.2 A g^{-1} to 10 A g^{-1}.

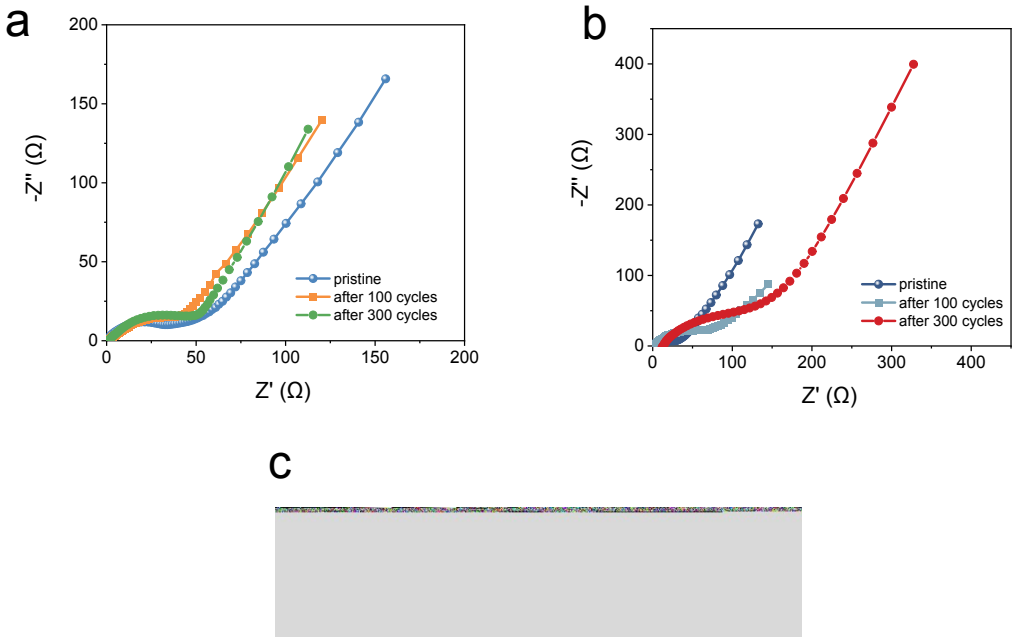

Fig. S38: EIS plots of ZHCs before and after cycling at 1 A g^{-1}. (a) Zn|AC ZHC with ZCS-Zn, (b) Zn|AC ZHC with bare Zn. (c) The equivalent circuit used to fit the EIS curves, where R_s is equivalent series resistance, CPE is double-layer capacitance, R_{ct} is charge transfer resistance and W is Warburg resistance.

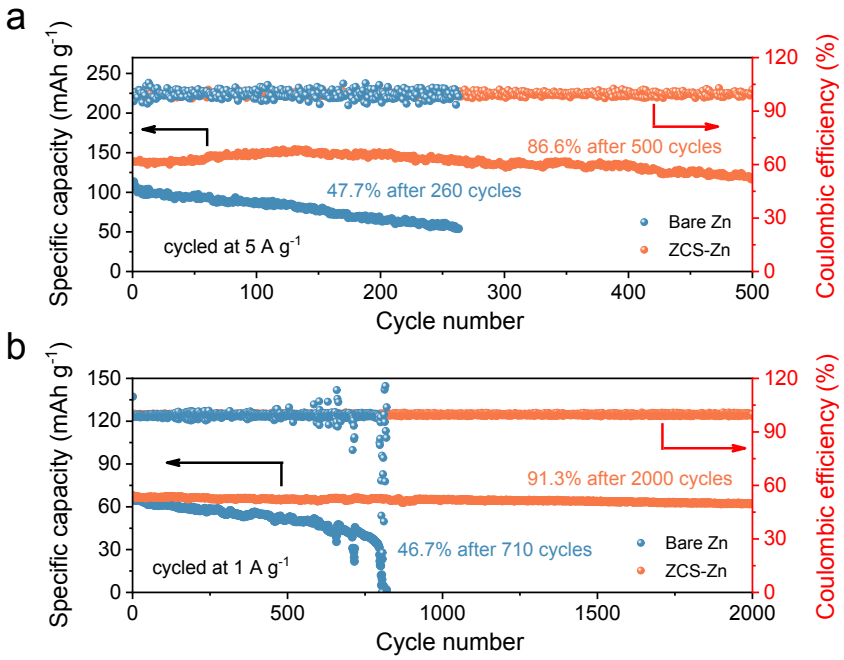

Fig. S39: The comparison of cyclic performance in (a) Zn|MnO_2 full cells and (b) Zn|AC hybrid capacitors with limited Zn (10 μm).

For long-term cycling at 5 A g^{-1}, Zn|MnO_2 full cell with ZCS-Zn displays a higher capacity retention of 86.6% after 500 cycles, compared with the severe capacity fading of more than 50% loss only after 260 cycles for full cell with bare Zn (Fig. S39a). In addition, the Zn|AC hybrid capacitor with ZCS-Zn could maintain a high capacity retention of 91.3% after 2000 cycles at 1 A g^{-1}, and this hybrid capacitor is still working stably in our lab. In contrast, the capacity of Zn|AC hybrid capacitor with bare Zn decreases by 46.7% only after 710 cycles (Fig. S39b).

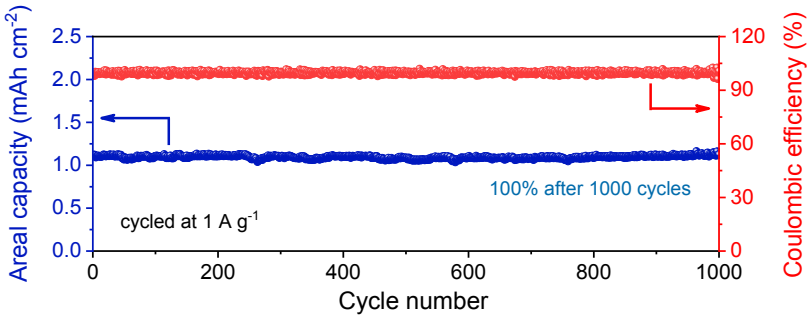

Fig. S40 Cyclic performance of ZCS-Zn|AC hybrid capacitors with limited Zn and a commercial-grade cathode loading mass of 26 mg cm^{-2}.

With a high loading of AC (26 mg cm^{-2}), the areal capacity of Zn|AC hybrid capacitor with ZCS-Zn could reach up to 1.12 mA h cm^{-2}, meaning a high Zn utilization ratio of 19.3% and a high N/P ratio about 5. Impressively, the Zn|AC hybrid capacitor with ZCS-Zn can work very well without apparent capacity fading during the 1000 cycles at 1 A g^{-1}, and this hybrid capacitor is still cycling stably in our lab.

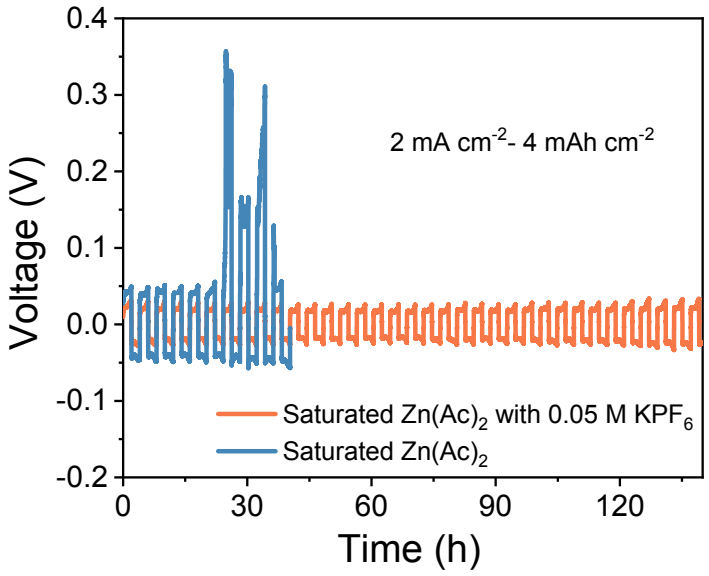

Fig. S41: Long-term galvanostatic cycling of Zn|Zn symmetrical cells in saturated $Zn(Ac)_2$ electrolyte with or without 0.05 M KPF_6 additive.

We further investigated the availability of the KPF_6 as electrolyte additive to induce the favorable ZCS on the surface of Zn in saturated $Zn(Ac)_2$ aqueous electrolyte. As shown in Fig. S41, Zn|Zn symmetric cells with 0.05 M KPF_6 additive exhibit the extended cycling life and lower polarization than that in saturated $Zn(Ac)_2$, demonstrating the versatility and flexibility of our strategy.

References

1. H. Li, C. Han, Y. Huang, Y. Huang, M. Zhu, Z. Pei, Q. Xue, Z. Wang, Z. Liu, Z. Tang, Y. Wang, F. Kang, B. Li and C. Zhi, *Energy Environ. Sci.*, 2018, **11**, 941-951.
2. A. H. Duan, W.-p. Chen, M. Fan, W.-p. Wang, S.-j. Tan, X. Chen, Q. Zhang, S. Xin, L. Wan and Y. Guo, *Angew. Chem. Int. Ed.*, 2020, **59**, 12069.
3. J. Hao, X. Li, S. Zhang, F. Yang, X. Zeng, S. Zhang, G. Bo, C. Wang and Z. Guo, *Adv. Funct. Mater.*, 2020, **30**, 2001263.
4. H. Qiu, X. Du, J. Zhao, Y. Wang, J. Ju, Z. Chen, Z. Hu, D. Yan, X. Zhou and G. Cui, *Nat. Commun.*, 2019, **10**, 5374.
5. T. Abe, H. Fukuda, Y. Iriyama and Z. Ogumi, *J. Electrochem. Soc.*, 2004, **151**, 1120-1123.
6. J. Lopez, A. Pei, J. Y. Oh, G. N. Wang, Y. Cui and Z. Bao, *J. Am. Chem. Soc.*, 2018, **140**, 11735-11744.
7. X. Xie, S. Liang, J. Gao, S. Guo, J. Guo, C. Wang, G. Xu, X. Wu, G. Chen and J. Zhou, *Energy Environ. Sci.*, 2020, **13**, 503-510.
8. K. Xu, Y. Lam, S. S. Zhang, T. R. Jow and T. B. Curtis, *J. Phys. Chem. C*, 2007, **111**, 7411-7421.
9. Y. Zhou, X. Wang, X. Shen, Y. Shi, C. Zhu, S. Zeng, H. Xu, P. Cao, Y. Wang, J. Di and Q. Li, *J. Mater. Chem. A*, 2020, **8**, 11719-11727.

10. Y. Wang, Y. Song and Y. Xia, *Chem. Soc. Rev.*, 2016, **45**, 5925-5950.

11. S. Liu, X. Ji, J. Yue, S. Hou, P. Wang, C. Cui, J. Chen, B. Shao, J. Li, F. Han, J. Tu and C. Wang, *J. Am. Chem. Soc.*, 2020, **142**, 2438-2447.

12. N. D. Lepley and N. A. W. Holzwarth, *Phys. Rev. B*, 2015, **92**, 214201.

13. Z. Zhao, J. Zhao, Z. Hu, J. Li, J. Li, Y. Zhang, C. Wang and G. Cui, *Energy Environ. Sci.*, 2019, **12**, 1938-1949.

14. K. Zhao, C. Wang, Y. Yu, M. Yan, Q. Wei, P. He, Y. Dong, Z. Zhang, X. Wang and L. Mai, *Adv. Mater. Interfaces*, 2018, **5**, 1800848.

15. W. Li, K. Wang, M. Zhou, H. Zhan, S. Cheng and K. Jiang, *ACS Appl. Mater. Interfaces*, 2018, **10**, 22059-22066.

16. M. Cui, Y. Xiao, L. Kang, W. Du, Y. Gao, X. Sun, Y. Zhou, X. Li, H. Li, F. Jiang and C. Zhi, *ACS Appl. Energy Mater.*, 2019, **2**, 6490-6496.

17. Z. Cai, Y. Ou, J. Wang, R. Xiao, L. Fu, Z. Yuan, R. Zhan and Y. Sun, *Energy Storage Mater.*, 2020, 27, 205-211.

18. H. He, H. Tong, X. Song, X. Song and J. Liu, *J. Mater. Chem. A*, 2020, **8**, 7836-7846.

19. K. Hu, X. Guan, R. Lv, G. Li, Z. Hu, L. Ren, A. Wang, X. Liu and

J. Luo, *Chem. Eng. J.*, 2020, **396**, 125363.

20. C. Deng, X. Xie, J. Han, Y. Tang, J. Gao, C. Liu, X. Shi, J. Zhou and S. Liang, *Adv. Funct. Mater.*, 2020, **30**, 2000599.
21. J. Hao, B. Li, X. Li, X. Zeng, S. Zhang, F. Yang, S. Liu, D. Li, C. Wu and Z. Guo, *Adv. Mater.*, 2020, **32**, 2003021.
22. J. Y. Kim, G. Liu, G. Y. Shim, H. Kim and J. K. Lee, *Adv. Funct. Mater.*, 2020, **30**, 2004210.
23. M. Zhou, S. Guo, G. Fang, H. Sun, X. Cao, J. Zhou, A. Pan and S. Liang, *J. Energy Chem.*, 2021, **55**, 549-556.
24. Y. Zeng, X. Zhang, R. Qin, X. Liu, P. Fang, D. Zheng, Y. Tong and X. Lu, *Adv. Mater.*, 2019, **31**, 1903675.
25. W. Dong, J.-L. Shi, T.-S. Wang, Y.-X. Yin, C.-R. Wang and Y.-G. Guo, *RSC Adv.*, 2018, **8**, 19157-19163.
26. Y. Tian, Y. An, C. Wei, B. Xi, S. Xiong, J. Feng and Y. Qian, *ACS Nano*, 2019, **13**, 11676-11685.
27. Z. Kang, C. Wu, L. Dong, W. Liu, J. Mou, J. Zhang, Z. Chang, B. Jiang, G. Wang, F. Kang and C. Xu, *ACS Sustainable Chem. Eng.*, 2019, **7**, 3364-3371.
28. Q. Zhang, J. Luan, L. Fu, S. Wu, Y. Tang, X. Ji and H. Wang, *Angew. Chem. Int. Ed.*, 2019, **58**, 15841.
29. W. Guo, Z. Cong, Z. Guo, C. Chang, X. Liang, Y. Liu, W. Hu and X. Pu, *Energy Storage Mater.*, 2020, **30**, 104-112.

30. L. Dong, W. Yang, W. Yang, H. Tian, Y. Huang, X. Wang, C. Xu, C. Wang, F. Kang and G. Wang, *Chem. Eng. J.*, 2020, **384**, 123355.

31. C. Wu, H. Tan, W. Huang, W. Li, K. N. Dinh, C. Yan, W. Wei, L. Chen and Q. Yan, *Adv. Funct. Mater.*, 2020, **30**, 2003187.

32. W. Xu, K. Zhao, W. Huo, Y. Wang, G. Yao, X. Gu, H. Cheng, L. Mai, C. Hu and X. Wang, *Nano Energy*, 2019, **62**, 275-281.

33. Z. Wang, J. Hu, L. Han, Z. Wang, H. Wang, Q. Zhao, J. Liu and F. Pan, *Nano Energy*, 2019, **56**, 92-99.

34. J. Zhao, J. Zhang, W. Yang, B. Chen, Z. Zhao, H. Qiu, S. Dong, X. Zhou, G. Cui and L. Chen, *Nano Energy*, 2019, **57**, 625-634.

35. L. Ma, S. Chen, N. Li, Z. Liu, Z. Tang, J. A. Zapien, S. Chen, J. Fan and C. Zhi, *Adv. Mater.*, 2020, **32**, 1908121.

36. C. Zhang, J. Holoubek, X. Wu, A. Daniyar, L. Zhu, C. Chen, D. P. Leonard, I. A. Rodríguez-Pérez, J. Jiang, C. Fang and X. Ji, *Chem. Commun.*, 2018, **54**, 14097-14099.

37. Y. Cui, Q. Zhao, X. Wu, Z. Wang, R. Qin, Y. Wang, M. Liu, Y. Song, G. Qian, Z. Song, L. Yang and F. Pan, *Energy Storage Mater.*, 2020, **27**, 1-8.

38. X. Zeng, J. Liu, J. Mao, J. Hao, Z. Wang, S. Zhou, C. D. Ling and Z. Guo, *Adv. Energy Mater.*, 2020, **10**, 1904163.

39. F. Wang, O. Borodin, T. Gao, X. Fan, W. Sun, F. Han, A. Faraone,

J. A. Dura, K. Xu and C. Wang, *Nat. Mater.*, 2018, **17**, 543-549.

40. Q. Zhang, J. Luan, Y. Tang, X. Ji and H. Wang, *Angew. Chem. Int. Ed.*, 2020, **59**, 13180.

41. H. Li, C. Xu, C. Han, Y. Chen, C. Wei, B. Li and F. Kang, *J. Electrochem. Soc.*, 2015, **162**, 1439-1444.

42. Y. Yin, S. Wang, Q. Zhang, Y. Song, N. Chang, Y. Pan, H. Zhang and X. Li, *Adv. Mater.*, 2020, **32**, 1906803.

43. T. Hoang, T. Doan, K. Sun and P. Chen, *RSC Adv.*, 2015, **5**, 41677-41691.

44. F. Ding, W. Xu, G. L. Gra, J. Zhang, M. L. Sushko, X. Chen, Y. Shao, M. H. Engelhard, Z. Nie, J. Xiao, X. Liu, P. V. Sushko, J. Liu and J. Zhang, *J. Am. Chem. Soc.*, 2013, **135**, 4450-4456.